Materials Science
of
Multilayer X-Ray Mirrors

Naureen Ghafoor

Linköping University
INSTITUTE OF TECHNOLOGY

Thin Film Physics Division
Department of Physics, Chemistry, and Biology (IFM)
Linköping University, SE-581 83 Linköping, Sweden

2008

All praises for Allah who is the entire source of knowledge and wisdom endowed to mankind and all respect for The Holy Prophet (PBUH) who is forever a torch of guidance

Abstract

This thesis treats the reflective and structural properties of multilayer structures. Soft X-ray multilayer mirrors intended as near-normal incidence reflective optics and polarizers in the water window (λ=2.4-4.4 nm) are the main focus. Such mirrors require multilayer periodicities between 1.2-2.2 nm, a large number $\sim$600 of multilayer periods (N), and atomically flat interfaces. Bi-metallic multilayers were deposited by dual-target magnetron sputtering on Si(001) substrates at ambient temperatures. Material combinations were chosen to maximize the theoretical reflectance based upon simulations. Hard and soft X-ray reflectivities, hard X-ray diffraction, high resolution transmission electron microscopy, and electron diffraction were used for structural characterization of the mirrors, whereas elastic recoil detection analysis and Rutherford back scattering spectroscopy were used for compositional analysis.

Geometrical roughness and intermixing/interdiffusion at the interfaces were investigated in connection with the impact of ion-surface interactions during growth of Cr/Ti, Cr/Sc, and Ni/V multilayers. This was achieved by comparing multilayers grown with or without high-flux low energy (E_{ion}<30 eV) ion assistance. The use of modulated ion assistance resulted in a substantial improvement of interface flatness and abruptness in each of the materials system. State-of-the art reflectivities of 2.1 %(Cr/Ti), 20.7%(Cr/Sc), and 2.7%(Ni/V) were achieved. It is found that Cr/Sc multilayers exhibit the highest quality and as many as 600 periods can be grown, but accumulation of local atomic distortions (jaggedness) limits the reflectivity at very large N. Moreover, it is shown that amorphous Cr/Sc multilayers exhibit smooth interfaces compared to nano-crystalline layers and that multilayers with period less than $\sim$2 nm are 'self healing', i.e., they re-gain smooth amorphous layers after morphological disturbances. Amorphization of Sc and Cr layers takes place below certain thicknesses. *Ab-initio* calculations indicate that the stabilization of the amorphous layer structure is due to a lowering of the total energy of the system by eliminating high energy incoherent interfaces between crystalline Sc and Cr.

Light element incorporation in Cr/Sc multilayers was investigated through residual gas pressure variation. It is shown that multilayers retain their structural and optical properties within the high vacuum range of 2×10^{-7}-to-2×10^{-6} Torr. The incorporation of 34 at.% nitrogen at a higher residual gas pressure ($\sim$$2\times10^{-5}$ Torr) resulted in highly textured understoichiometric CrN_x/ScN_y multilayers. As a result of nitrogen incorporation, interface widths as small as 0.29 nm, and near-normal incidence reflectivity enhancement (at λ=3.11 nm) by 100 % (compared to pure Cr/Sc multilayers) was achieved. Light element incorporation was also found to be advantageous for the thermal stability of the multilayers. *In-situ* hard X-ray reflectivity measurements performed during isothermal annealing in the temperature range 25-900 °C has shown that understoichiometric CrN_x/ScN_y are stable up to 350 °C. As an alternative route to metallic multilayers, single crystal CrN/ScN superlattices, grown by reactive sputtering in N atmosphere onto MgO(001), were also investigated. The superlattice synthesis at 735 °C, resulted in highly abrupt interfaces with minimal interface widths of 0.2 nm. As-deposited superlattices with only 61 periods showed an absolute soft X-ray reflectance of 6.95% at λ=3.11 nm as well as very high thermal stability up to 850 °C.

.

Populärvetenskaplig Sammanfattning

Denna avhandling behandlar syntes, analys, och materialvetenskap rörande så kallade multi-lagerspeglar för mjuk röntgenstrålning. Speglarna är lämpade som optiska komponenter för instrument såsom röntgenmikroskop i våglängdsområdet 2,4 nm till 4,4 nm, även kallat vatten-fönstret.

Tack vare de senaste decenniernas stora teknologiska och vetenskapliga framsteg i att framställa mycket intensiva källor för mjuk röntgenstrålning, såsom tex synkrotronljuskällor, frielektronlasrar, och plasmagenererade källor, är det nu tänkbart att utnyttja denna strålning till nya tillämpningar som tidigare inte varit möjliga. Några exempel är; röntgenmikroskopi av biologiska preparat med upplösning ca 1/100 av det som är möjligt med synligt ljus, fotolitografi av strukturer endast några tiotals nm stora, samt för studier av dynamiska förlopp inom kemi och biologi med en tidsskala på femtosekundsnivå eller kortare. Även inom astronomin finns det ett stort intresse av att avbilda avlägsna naturliga röntgenkällor. För dessa ändamål krävs högupplösande optiska instrument med så få förluster som möjligt. Tyvärr uppvisar de flesta material ett brytningsindex för mjukröntgen som är mycket nära 1 samt en kraftig stor absorption. Detta gör att det inte är möjligt att utforma de optiska elementen, dvs linser och speglar, på konventionellt sätt i sådana instrument. För att uppnå hög reflektans för mjuk röntgen-strålning vid nära normalt infall utnyttjas därför möjligheten att skapa konstruktiv interferens mellan röntgenvågor som reflekterats i ett stort antal mellanytor inne i en lagrad struktur av nanometertunna skikt, en så kallad interferensspegel, här kallad multilagerspegel.

Det finns flera stora utmaningar för att lyckas tillverka multilagerspeglar. Först och främst måste man hitta materialkombinationer som ger upphov till reflektion i mellanytorna mellan materialen men som inte samtidigt absorberar all röntgenstrålning. Dessutom måste materialen gå att belägga på varandra i flera hundra tunna lager, vart och ett endast ca 1 nanometer tjockt, med en ytojämnhet om endast några tiondels nanometer. Den absoluta tjockleks precision i varje lager som krävs för att uppnå perfekt konstruktiv interferens ligger på femtometernivå. Detta kräver stora kunskaper inom såväl materialvetenskap som beläggning av extremt tunna filmer och är huvudämnet för denna avhandling.

I det här arbetet har fyra olika typer av multilagerbeläggningar undersökts: krom/titan (Cr/Ti), krom/skandium (Cr/Sc), nickel/vanadin (Ni/V) samt kromnitrid/skandiumnitrid (CrN / ScN). Materialvalen har baserats på teoretiska beräkningar som visat att dessa materialsystem genererar mycket god reflektans i vattenfönstret. Varje kombination av metaller är optimal för en specifik våglängd och de individuella lagertjocklekarna måste optimeras teoretiskt för varje enskilt fall. Beläggningarna av speglarna gjordes under lågt tryck, ca 10^{-6} atmosfärer av argon och kväve, med så kallad magnetronsputtring där flödet av metallatomer noggrant kunde kon-trolleras med hjälp av datorkontrollerade slutare. Under arbetets gång utvecklades en ny teknik, som med hjälp av ett stort flöde av lågenergetiska joner till den växande filmen, resulterar i en tydlig förbättring av metallskiktens jämnhet. Genom att förfina metoden, så att jonflödet regleras under beläggningen av varje skikt, har även mellanytorna kunnat göras mer abrupta. I förlängningen ledde dessa forskningsresultat till att multilagerbeläggningar med överlägsen reflektans kunde framställas. Till exempel uppmättes rekordreflektansen 20% för röntgenstrål-ning av våglängden 3,11 nm för ett Cr/Sc multilager som tillverkats med sex hundra 0,605 nm tjocka Cr-lager varvade med lika många 0,985 nm tjocka Sc-lager. För Cr/Ti och Ni/V upp-nåddes reflektanserna 2,4% för 2,74 nm våglängd respektive 2,7% för 2,42 nm våglängd, vilken ännu är det högsta rapporterade värdet för så kortvågig röntgenstrålning.

För Cr/Sc multilager har vi visat att lagren som beläggs har en oordnad, så kallad amorf, struktur av metallatomerna som har sitt ursprung i att multilagrets totala energi kan sänkas om mellanytor mellan kristallint Cr och kristallint Sc kan undvikas.

Studier av effekterna av kväveupptag hos Cr/Sc multilagerspeglar under sputtrings-processen har lett till ökad förståelse av materialsystemet. Till exempel har vi visat att kvävet

framförallt binder till de inre regionerna av Sc och inte så mycket till Cr-lagren eller i mellanytorna. Med kväve i strukturen har vi gjort speglar som tål höga temperaturer, vilket är av stor betydelse för tillämpningar baserade på högintensiva ljuskällor. Så kallade supergitter, dvs multilager tillverkade i form av en enda kristall med lagringen av material inom själva kristallen, visade sig vara mycket stabila upp till 850 °C med bibehållen röntgenreflektans. Supergitter har dock den svagheten att de är svåra att belägga på substrat för optiska komponenter eftersom de kräver ett kristallint substrat och hög beläggningstemperatur. Ytterligare ett viktigt resultat är därför att polykristallina Cr/Sc multilagerspeglar med 34 atom-% kväve i strukturen, som tillverkats vid rumstemperatur på vanliga kiselsubstrat, visade sig stabila upp till 250 °C och gav en förbättrad mjukröngenreflektans jämfört med rena Cr/Sc multilagerspeglar.

Preface

This doctorate thesis is a result of my PhD studies from 2004 to 2008 at the Thin Film Physics Division of the Department of Physics, Chemistry, and Biology (IFM) at Linköping University. Research on the development of soft X-ray multilayer mirrors was initiated about ten years ago at the department and I have been involved in this work since my Master's diploma studies in 2002. The work has been presented at nine international conferences and is published in several scientific journals. At the end of this thesis seven of my articles, most related to the present work, are included.

Publications Included in this Thesis and My Contribution

Paper I
"Atomic scale interface engineering by modulated ion assisted deposition applied to soft X-ray multilayer optics", F. Eriksson, N. Ghafoor, F. Schäfers, E. M. Gullikson, S. Aouadi, S. Rohde, L. Hultman, and J. Birch, *submitted* (2008)

      I performed TEM characterization and took active part in writing the manuscript.

Paper II
"Effects of ion-assisted growth on the layer definition in Cr/Sc multilayers", N. Ghafoor, F. Eriksson, P. O. Å. Persson, L. Hultman, and J. Birch, Thin Solid Films **516**, 982 (2008)

      I grew all the samples, performed TEM and XRD analyses, and wrote the article with the assistance of the co-authors.

Paper III
"Incorporation of nitrogen in Cr/Sc multilayers giving improved soft x-ray reflectivity", N. Ghafoor, F. Eriksson, E. M. Gullikson, L. Hultman, and J. Birch, Appl. Phys. Lett., **92**, 091913 (2008)

      I did all the experiments except ERDA and SXR analyses, and wrote the paper with assistance from the co-authors.

Paper IV
"Effects of O and N impurities on the nanostructural evolution during growth of Cr/Sc multilayers", N. Ghafoor, F. Eriksson, A. Mikhaylushkin, I. Abrikossov, E. M. Gullikson, M. Beckers, U. Kressig, L. Hultman and J. Birch, *submitted* (2008)

      I actively contributed in planning the experiments, designed and grew sophisticated stacked multilayers structures, performed extensive TEM work and HXR analyses, and I wrote the paper together with the co-authors.

Paper V
"Reflectivity and structural evolution of Cr/Sc and nitrogen containing Cr/Sc multilayers during thermal annealing", F. Eriksson, N. Ghafoor, L. Hultman, and J. Birch, *submitted* (2008)

      I participated in planning of the experiments, designed and grew the samples, performed all TEM characterization and took active part in analyses and writing of the final manuscript.

Paper VI
"Single crystal CrN/ScN superlattice soft X-ray mirrors: Epitaxial growth, structure, and properties", J. Birch, T. Joelsson, F. Eriksson, N. Ghafoor, and L. Hultman, Thin Solid Films, **514**, 10 (2006)

      I took part in SXR measurements and participated in writing the final manuscript.

Paper VII
"Interface engineered ultra-short period Cr/Ti multilayers as high reflectance mirrors and polarizers for soft X-rays of λ=2.74 nm wavelength", N. Ghafoor, P. O. Å. Persson, F. Eriksson, F. Schäfers, and J. Birch, Appl. Opt. **45**, 137 (2006)

      I designed and grew the samples, performed all the characterization, made the analysis, and wrote final manuscript with the help of the co-authors.

Related Publications

Paper VIII
"Interface Engineering of Short-period Ni/V multilayer X-ray mirrors", F. Eriksson, N. Ghafoor, F. Schäfers, E. M. Gullikson, and J. Birch, Thin Solid Films, **500**, 84 (2006)

Paper IX
"Role of B_4C on structure, optical performance, and thermal stability of short period soft X-ray multilayers" N. Ghafoor, F. Eriksson, E. M. Gullikson, and J. Birch, *in manuscript* (2008)

Paper X
"Influence of concurrent ion-bombardment during magnetron sputter deposition of Mo/Si multilayers", J. Romero, N. Ghafoor, F. Eriksson, and J. Birch, *in manuscript* (2008)

Conference Contributions

During my PhD studies I have had the opportunity to attend several international conferences. Some of the conferences where I personally presented my research are listed here.

- "Soft X-ray Cr/Sc multilayer mirrors: effects of B_4C, O and N impurities", The 9th international conference on Physics of X-ray Multilayer Structures (PXRMS), Montana, USA, Invited talk, O-2.1 (2008)

- "Ion assisted growth of short period Ni/V multilayers", The 15th International Summer School on Vacuum Electron and Ion Technology (VEIT), Sozopol, Bulgaria, Contributed talk, OP-07 (2007)

- "Cr/Sc Multilayer Mirrors: Influence of impurities on amorphous-to-crystalline layer transformation and optical properties", The 17th International Vacuum Congress (IVC), Stockholm, Sweden, Contributed talk, TFS01-O4 (2007)

- "Cr/Sc X-ray Multilayer Mirrors: Influence of impurities on structure and performance of Cr/Sc multilayer mirrors", Advances in X-ray/EUV Optics and Components II, Optics and Photonics (SPIE), San Diego, USA, Contributed talk, 6705-10 (2007)

- "Interface engineered Cr/Sc multilayer mirrors for normal incidence reflection of soft X-rays range at Sc (λ=3.1 nm) absorption edge", International Summer School on Surfaces, Thin Films, Nanostructures and Applications (CIIT-ISESCOC), Lahore, Pakistan, Contributed talk, O-22 (2006)

- "Roughness propagation in short-period Cr/Sc and Cr/Ti multilayers", The 8th international conference on Physics of X-ray Multilayer Structures (PXRMS), Sapporo, Japan, Contributed talk, S7-04 (2006)

- "Nanostructural evolution of interface engineered Cr/Ti Multilayers", The International Conference on Metallurgical Coatings and Thin Films (ICMCTF), San Diego, USA, Contributed talk, F3-03 (2005)

- "Interface engineered Ti/Cr multilayer mirrors for normal incidence reflection of soft X-ray range at Ti-*2p* edge", International Conference on Thin Films (ICTF-13/ACSIN-8), Stockholm, Sweden, Contributed talk, O-137 (2005)

- "Ti/Cr multilayer mirrors for normal incidence in the soft x-ray range at the Ti-edge", The 7th international conference on Physics of X-ray Multilayer Structures (PXRMS), Sapporo, Japan, Poster presentation, P2-09 (2004)

.

Acknowledgements

I never think of the future. It comes soon enough. Albert Einstein

So, the time has arrived for me, so to say, to wrap-up last six years of my work. Where my mind, in these long hours of writing final manuscripts and thesis, is linking several dispersed concepts of multilayer science, it is also rewinding different stages of PhD. All the excitements when I had just seen nice reflectivity peaks in *Asterix*, or wonderful layered structures in *Galadriel*, and occasional frustrations when B_4C was so stubborn to start and *ADAM* had just refused to listen me; all feelings are now equally great memories. And above all this time is reminding me every single person involved in my work and/or has made my time joyful at *IFM* or outside work. Though, my vocabulary here is very limited, I would give a try to express my gratitude to,

Jens Birch-my wonderful supervisor, your guidance, encouragement and endless patience during all these years has made me accomplish this thesis. Your fundamental knowledge in *literally* everything and philosophy of transferring as much knowledge as possible to everyone has always inspired me. Thanks Jens! for believing in me and giving me so much freedom in work. It has been great to have you as my supervisor. Thanks for, all the scientific discussions, helping me in every little thing, and for all the fun-travelling around the world.

Lars Hultman-my group leader, for creating an inventive working environment in the group and for having an encouraging concern in my research. Although, I have had hard times to understand a high level microscopy language, it has been rewarding to have all 'instant' discussions with you.

Fredrik Eriksson-my ancestor in the field, for his significant contribution in 'getting started' me with the sputtering, simulations, and more or less everything around. Thanks Fredrik, for great friendship we have had! it was really fun times at conferences, on summer trips and of course during *the driving lessons.*

Per Persson-the microscopy guru, you simply, *never* have said no to me weather it concerns solving TEM issues or listening my general problem over the coffee table.

Co-Authors-I would like to acknowledge all the people who have helped me in collecting data and writing articles, presented in this thesis.

I am also grateful to **Carina Höglund** and **Andy Aquilla** for giving me favours in measurements.

Kalle Brolin, Thomas Lingefelt & Inger Eriksson, You all are masters in your fields. We cannot be successful without your help. Thanks a lot for keeping us working.

Petter Larsson, I honestly think that you are too skilled to solve Naureen-troubles, and I truly appreciate all your help in the lab, especially to make 'B$_4$C magnetron' to work.

I am thankful to all the past and present members of the **Thin Film Physics, Plasm** & **Coating Physics, and Nanostructured Materials Divisions.**for the cooperation and creating great working environment.

Anders Elfving for a very nice friendship since my first day at IFM.& **Ming Zhao** for always being there whenever I need help.

Axel Flink, for a sincere friendship. Thanks for introducing me to the Swedish summer and Christmas, for all the fun trips and most of all for giving me company during the course of writing.

Halldora, for providing me home away from home.

Uzma Khalique, without your support I would not have been in Linköping.

Birch's family, I liked being with you all....

My Family, for all the support and encouragement especially from **my Parents**, you have always been a great source of strength.

Naureen

.

Contents

Chapter 1

Introduction

A desire to enable X-ray vision and X-ray imaging of nm sized objects has established a rapidly growing field of research, covering all areas from X-ray source development to X-ray imaging and spectroscopy instrumentation [1]. Since 1895, soon after the discovery of X-rays, the advancement in X-ray sources has been a non-stop technology and X-rays which, at that time, were produced in a small vacuum tube are now also generated at large synchrotron radiation facilities with 15 orders of magnitude higher average spectral brightness than their first production. The state-of-the-art is the "X-ray free-electron laser" which allows high-brilliance sources of coherent X-rays. In recent years there has also been a rising swell of research devoted to the development of table top X-ray sources based on Laser produced plasma (LPP) [2] and Čerenkov radiation [3] and even on table top free-electron laser [4] source. However, development of instruments that can take advantage of these state-of-the-art X-ray sources is hindered by the absence of appropriate X-ray optical elements particularly in soft X-ray and EUV region where natural crystals are not available for optical collection, collimation, and convergence of X-rays. These optical elements are indispensable for building, especially soft X-ray microscopes, spectrometers, polarimeters or polarizers, EUV lithography tools required in the electronic industry, soft-X-ray diagnostic of high temperature plasma, and also for exploring the fascinating world of cosmology and astronomy by solar imaging instruments or deep space telescopes operating at wavelengths of natural X-ray sources [5]-[9].

For soft X-ray and EUV wavelengths no material is absorption free and due to low refractive index reflectance of all materials is vanishingly small and conventional optical elements, lenses or thin film coated mirrors are not applicable. An exception to this, is total external reflection of X-rays at very low incident angles, which allows to use large sized singly coated grazing incident mirrors as converging optics. Nevertheless, from a technological point of view normal-incidence optics are currently desired as they have many advantages over the grazing ones. For example, since all X-ray wavelengths are reflected below the critical angle, wavelength dispersion, i.e., reflectance of certain wavelength only at a specific angle, with high spectral resolution, can only be achieved at higher angles by specifically designed mirrors. Moreover, in comparison to grazing incidence mirrors normal incidence mirrors are smaller in size, have higher efficiency due to a large collection area and above all the size of the mirror and radiation collection geometry enable the possibility to build compact, small sized, laboratory instruments. However, this requires a highly reflective surface which can only be accomplished by multilayer interference coatings [10] often referred as multilayer mirrors. Multilayer mirrors are formed by depositing hundreds of alternating layers of usually two materials of dissimilar refractive indices that form long-term stable interfaces.

Today, the major challenge in the multilayer mirror field is to find optically and chemically compatible materials for consecutively growing up to thousands of sub-nm thin layers with abrupt and sharp boundaries. Moreover, the nucleation and growth methodology of metal

multilayers have not been fully understood especially when multilayers are grown under highly non-equilibrium conditions with kinetic limitations. Another challenging area for the multilayer community is the methods of detailed multilayer characterization of buried interfaces. All these matters are, to some extent, addressed in this thesis and solutions to a number of so far unsolved research issues which are essential for mirror reflectivity and thermal stability are discussed

This thesis is compiled into eight chapters. The next chapter deals with the general description of X-ray reflection from a multilayer and also the most commonly used terminologies in the field are introduced. Material selection and mirror design rules followed in this work are also described. Chapter 3 is a detailed outlook of metal multilayer growth related issues. Several characterization methods have been used during this work. Chapter 4 deals with the techniques and kind of information revealed from each of the analyzing technique. In Chapter 5 multilayer roughness evolution during growth is discussed with some examples of the present work. The work during the last two years was related to the study the effects of impurity incorporation into the multilayers and is shortly discussed in Chapter 6. Chapter 7 presents a summary of the papers constituting this thesis, and Chapter 8 is devoted to some related, yet unpublished, results and an outlook for future experiments.

Chapter 2

Soft X-ray Multilayer Mirrors

In multilayer mirrors, reflection occur at each interface due to the discontinuity in the complex refractive index, η, of the constituting materials. By tailoring the layer thicknesses, the reflectivity, R, versus wavelength, λ, or R versus grazing incidence angle, θ, can be designed to follow a curve of any desired shape. Multilayer mirror principle, materials selection criterion, and design are described in this chapter. In addition, concepts of various interfacial roughnesses and imperfections are introduced.

The spectral region, extending from a wavelength of roughly $\lambda = 0.01$ nm to about 50 nm, is generally (although the boundaries are diffuse) categorized as hard X-rays (HXR), $\lambda < 0.5$ nm, soft X-rays (SXR), $0.5 < \lambda < 10$ nm, and extreme ultraviolet radiation (EUV), $10 < \lambda < 50$ nm [11]. EUV radiation is vital for smaller wavelength lithography in the electronic industry, while the region of particular interest for the biosciences is ranging from the oxygen absorption edge, $\lambda = 2.4$ nm, to the carbon absorption edge, $\lambda = 4.4$ nm called "the water window". Here the X-ray radiation is absorbed by carbon but transmitted through oxygen, and this high natural contrast is indeed very attractive for imaging biological specimens in their natural aqueous environment [2],[12],[13],. Although, most of the discussion in this thesis is generally true for all X-ray wavelengths, the research presented here is mainly focused on normal incidence soft X-rays reflective optics for water window applications and oblique incidence polarizers and analyzers for soft X-ray polarimetry [14].

2.1 Multilayer X-ray Mirrors

X-ray multilayer mirrors are based on the principles of constructive interference in extremely thin layers of material, with a large contrast in X-ray refractive indices, deposited on a mirror surface. A schematic of periodic multilayer mirror is shown in Fig. 2-1, for a stack of (in this case) two alternating materials A and B. The parameters that can be varied in a periodic multilayer are the substrate, the two different layer materials, A and B, the order of the layer (ABAB.. or BABA..), the total number of bilayers or multilayer period, N, and the individual layer thicknesses, D_A and D_B. Among the multilayer community, multilayer period, $\Lambda = D_A + D_B$, and the top-layer-to-bilayer thickness ratio, $\Gamma = \dfrac{D_B}{D_A + D_B}$, are the most commonly used expressions for differentiating in-between multilayers.

Bragg's law [15] explains the condition of diffraction by an ordered array of atoms, in a crystal as,
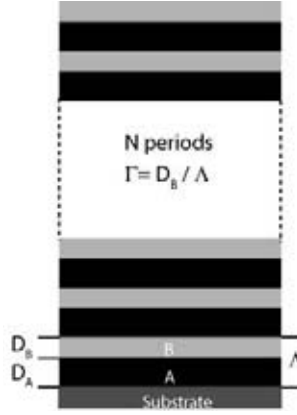
Figure 2-1: Schematic of an ideal multilayer with a periodic sequence of alternating layers of A and B materials, for N number of total periods.

$$m\lambda = 2\Lambda \sin\theta \tag{2.1}$$

where Λ is the spatial periodicity, λ is the X-ray wavelength, m is an integer called the order of diffraction, and θ is the angle of X-ray incidence measured from the normal to the reflecting plane. In multilayers mirrors, which are one dimensional analogues of 3D crystals, mirror reflection occurs at each interface due to the discontinuity in the complex refractive index, η, of the two constituting materials. The structure of a multilayer in the direction normal to the layers can be deduced from a measured reflectivity curve as shown in Fig. 2-2. High reflectivity can be obtained from a multilayer when the periodicity is such that reflections from all surfaces occur in phase. In contrast to visible light, η is slightly less than unity for all materials in the X-ray wavelength region and can be expressed as,

$$\eta = 1 - \delta + i\beta \tag{2.2}$$

To account for the average refractive index of two materials Bragg's law can be modified [1] as,

$$m\lambda = 2\Lambda \sin\theta \sqrt{1 + \frac{(1 - \bar{\delta})^2 - 1}{\sin^2\theta}} \tag{2.3}$$

where $(1 - \bar{\delta})$ is the average real part of the refractive index which for bilayers is:

$$\bar{\delta} = \frac{d_A\delta_A + d_B\delta_B}{d_A + d_B} \tag{2.4}$$

δ_A and δ_B are the dispersion coefficients of the layer A and B respectively. $\bar{\delta}$ is on the order of 10^{-5} in solid materials and only around 10^{-8} in air. The imaginary part β, which accounts for absorption, is usually very small for HXR but significantly higher for SXR wavelengths. This means that the X-ray wavelength is slightly shorter inside the material than in air or vacuum.
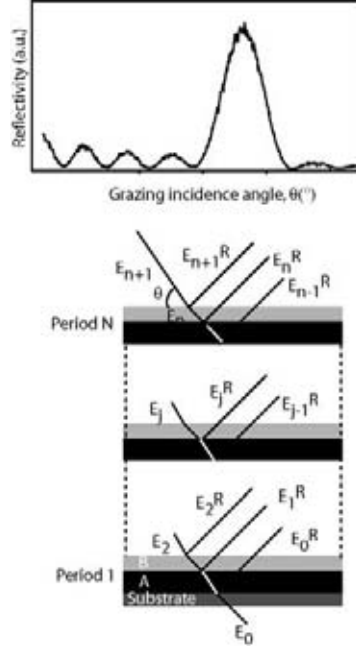
Figure 2-2: An optical model [16] for X-ray reflection from a multilayer containing N periods and n+1 interfaces. X-ray reflections from the substrate, (n = 0), till the vacuum-multilayer interface (n+1) are shown. A typical reflectivity curve versus the angle θ, is shown on the top. Peak reflectance corresponds to the angle where reflections from all interfaces is in phase.

A linearization of Eq. 2.3 relates Λ to the grazing incidence angle θ and Bragg order m as,

$$m^2 = 4\frac{\Lambda^2}{\lambda^2}[\sin^2\theta + \{(1-\bar{\delta})^2 - 1\}]$$ (2.5)

By utilizing the reflectivity measurements (Fig. 2-2), the multilayer period can thus be determined from the slope, $4\frac{\Lambda^2}{\lambda^2}$, of the $\sin^2\theta$ versus m^2 plot. For normal incidence, $\theta = 90°$, the above Eq. reduces to,

$$\Lambda = \frac{m\lambda}{2\bar{\eta}}.$$ (2.6)

This implies that the multilayer period Λ, which gives constructive interference, is thus slightly smaller than half of the X-ray wavelength for the first order reflection (m = 1) at normal incidence. For water window applications these periodicities are just 1.2-2.2 nm, and individual layers are sub-nm thin.

In addition to normal incidence, multilayers were also studied at Brewster's angle, θ_B,

where p-polarized part of X-rays become completely transmitting and only s-polarized light reflects, thus mirror act as a polarizer [11]. For X-rays θ_B is slightly less than 45°, which implies slightly larger periods (Eq. 2.3) for polarizing mirrors compared to normal incidence mirrors.

2.2   Materials Selection for Soft X-ray Mirrors

A large difference in electron density of a high and low atomic number, Z, between the layer materials provides refractive index contrast and can be useful as a guide for material selection. However, a more detailed study of the optical properties expands the possibilities. For the multilayers discussed in this thesis, the material selection was based on the combined optical properties as a function of wavelength of the multilayer constituents.

In general, optical theory implies that at normal incidence reflectivity, $R(\theta) = I(\theta)/I_0$, i.e. the fraction of the incident X-ray intensity reflected at normal incidence, $\theta = 90°$, from ideal single interface is approximately,

$$R \approx \frac{(\Delta\delta)^2 + (\Delta\beta)^2}{4} \tag{2.7}$$

where $\Delta\delta$ and $\Delta\beta$ are the differences in dispersion and extinction coefficients between the two layer-materials, respectively [11]. These coefficients are in turn related to the operating wavelength and the complex atomic scattering factors as,

$$\delta = \frac{N_a r_e \lambda^2}{2\pi}(f_o + f\,') \tag{2.8}$$

and,

$$\beta = \frac{N_a r_e \lambda^2}{2\pi} f\,'' \tag{2.9}$$

here, N_a is the atomic density, r_e is the Thompson scattering length, f_o is the Thompson scattering factor and $f\,'$ and $f\,''$ are the real and imaginary dispersion correction factors to the Thompson scattering factor. The extinction coefficient β can also be defined as,

$$\beta = \frac{\mu\lambda}{4\pi}, \tag{2.10}$$

where, μ^{-1} accounts for the attenuation of X-rays to a characteristic length of $1/e$, in a material and is called absorption coefficient.

Predominantly, the materials selection was made for mirrors apt for line-emission sources like the LPP or Čěrenkov radiation sources. Therefore, the materials having their absorption edges within the water window like transition metals Ti, V and Sc were picked for mirror design. An intention behind choosing these materials was the "anomalous dispersion" of X-rays at the corresponding edges where the refractive index becomes slightly more than unity, which in turn, can be utilized to get the enhanced reflectance.

For example, anomalies in δ and β for titanium, at the Ti-*2p* absorption edge ($\lambda = 2.74$ nm, $E = 452$ eV) are illustrated in Fig. 2-4 (a). In order to select the second layer material with Ti the optical constants, δ and β, for several other elements were plotted in the same graph for $\lambda = 2.74$ nm, as shown in Fig. 2-4 (b), and Eq. 2.7 was partially used to pick few materials which have given maximum difference in $\Delta\delta$ with Ti.

The condition, that $\Delta\beta$ has to be maximum does not entirely hold true when combined reflections from a large number of interfaces are desired. In that case a large β will lead to

Figure 2-3: Periodic table of the elements. The highlighted transition metals and light elements are considered in this thesis for soft X-ray multilayer mirror fabrication.

significant absorption of penetrated X-rays according to Eq. 2.10 and only reflection from a few interfaces at the top will contribute to the reflected intensity. Hence, the maximum $\Delta\beta$ selection rule was relaxed and the second materials were also selected from the low β region and the probability of higher reflectance was then increased by designing mirrors with a large number of interfaces $\backsim 200 - 300$.

As shown in Fig. 2-4 (b), there are a few materials with low β, and with $\delta < 0.006$, which fulfilled the above criterion of selection. However, strongly magnetic materials like Fe and Co were discarded due to the expected difficulties for deposition. The remaining materials (Ni, Zn, Mn, and Cr) were simulated with Ti for maximum reflectance for a semi infinite multilayer at normal incidence. As illustrated in the Fig. 2-5 the highest reflectivity of $\backsim$46%, was calculated for Cr/Ti multilayers, due to a lower overall absorption in this materials system. The simulations also suggested that Ni/Ti is an alternative or even better material combination, because of the higher contrast in δ, but, high absorption limits the reflectivity for large N ~ 300 multilayers [17] . In my work, the Cr/Ti multilayers selection was based on the research interest of studying multilayer systems with a large number of interfaces and to obtain maximum achievable reflectivity.

In addition to optical contrast the tendency of miscibility, chemical diffusion or reactions of the material combinations should also be considered while choosing the materials. For example C/Ti multilayer combination though not suggested by optical properties have shown higher reflectivities due to higher quality of layered structure, compared to optically suggested Cr/Ti multilayers [18]. These aspects of materials selection are discussed in the context of roughness evolution in Chapter 5.
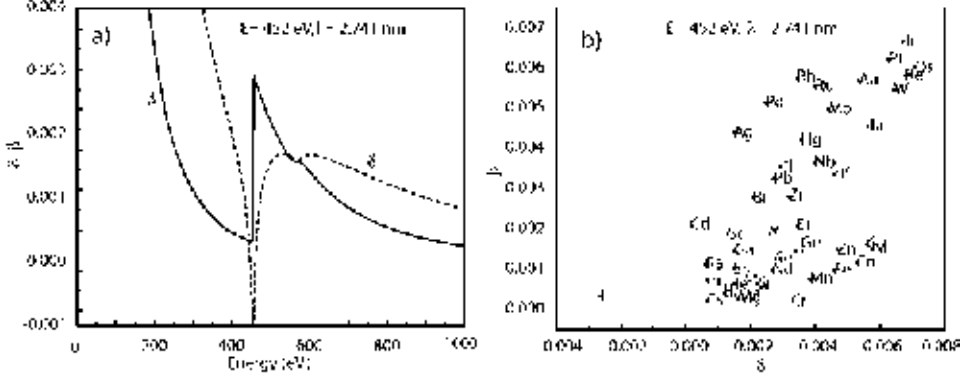
Figure 2-4: (a) Discontinuities in Ti optical constants, δ, and β, at $2p$ absorption edge. The values of δ are negative close to an absorption edge which made the η to be slightly more than unity.(b) 2D- $\delta\beta$ plot for variety of high refractive index materials, than Ti, at Ti-$2p$ edge.
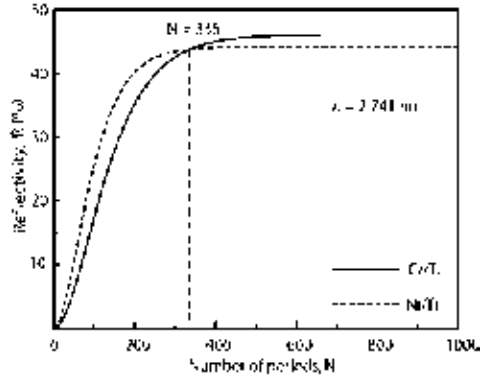
Figure 2-5: Simulations showing the reflectivity evolution versus number of periods for Cr/Ti and Cr/Ni materials systems. The effect of higher β of Ni becomes dominant for $N > 300$.

2.3 Multilayer Design

Multilayer design implies the determination of the multilayer period, Λ, the top layer-to-bilayer thickness ratio, Γ, and the total number of bilayers, N. By using the optical constants from the database CXRO [19] and IMD [20] software, which is a computer program for modelling the optical properties of multilayer films, the combination of Λ and Γ giving the highest reflectance for a given materials system were found. Required input parameters for such simulations were the selected elements with known optical constants (including substrate material), the order of materials, the operating wavelength, and the incidence angle. The order of materials, which in turn determines Γ, should be chosen to obtain highest optical contrast between vacuum ($\eta_0 = 1$) and the top layer material, to achieve maximum reflectance according to Eq. 2.7. However, the chemical reactivity of the materials has to be taken into account, e.g., in the Cr/Ti system, Cr was chosen as the top layer because of its ability to form a passive oxide layer over the highly reactive Ti.

Once Λ and Γ were chosen, the next design step was the determination of the total number of periods needed to obtain the maximum theoretical reflectance. Since the reflectivity from a single interface (Eq. 2.7) is typically on the order of $10^{-4}-10^{-6}$ at near-normal incidence, in-phase reflection from 10^2-10^3 interfaces is required to reach maximum reflectivity;thereafter, absorption in the multilayer stack limits the reflectivity. The simulations were performed to obtain N corresponding to saturation reflectance. A maximum reflectance by no means is the only requirement to determine N in periodic multilayer structures which are wavelength dispersive mirrors, act as narrow-band pass filters and need as high reflectance as possible at a single wavelength. Alternatively, aperiodic multilayers are used as broad-band pass filters and are normally designed to reflect large range of wavelengths with uniform reflectivity. The selection rule [21] for estimating the effective number of bilayers with respect to the spectral resolving power is,

$$\frac{\Delta\lambda}{\lambda} \approx \frac{1}{mN} \qquad (2.11)$$

2.4 Real Interfaces and Associated Roughness

Until now, it has been assumed that each interface in a multilayer is chemically abrupt and atomically flat without any irregularities. By definition, such an interface is known as an "ideal interface" and physically have an infinitely small width of the interface. However, in reality, such interfaces never exist. Several phenomena contribute to widen the interface for example, thermal diffusion, intermixing, atomic irregularities, impurities incorporation, structural transitions, induced stresses etc. Whatever the phenomenon is, an increase in the interface roughness drastically deteriorates the reflectivity of the multilayer. The word "roughness", frequently used for uneven surfaces, has multifaceted interpretation when it is linked to an interface and gets even further complicated when it is interpreted for several consecutive interfaces in a multilayer system.

The simplest way of defining the roughness at an interface is to consider whether the transition of refractive index at the boundary of the two materials, is abrupt, continuous, step-like or a combination of these. This, in turn, gives rise to an interface profile function, $g(z)$, usually defined as the normalized average of the refractive index along the growth direction, z, [23] and is mathematically represented as, $g(z) \longrightarrow 1, z \longrightarrow \infty$. The spatial derivative of the profile function is,

$$f(z) = \frac{g(z)}{dz}, \qquad (2.12)$$

A more common measure for a transition region is the "interface width, 2σ," an average amplitude of surface height fluctuations, which is related to the interface profile as,

$$\sigma = \int z^2 f(z) dz \tag{2.13}$$

Most generally, the deviation from an ideal interface is categorized as an intermixed (chemically diffuse) and/or rough (physically distorted) interface. The σ for these three types of multilayers is shown in Fig. 2-6 along with their corresponding profile functions. For an ideal interface, $g(z)$ is a unit step function characterized by infinitesimally thin interface widths ($\sigma = 0$) while for the intermixed interfaces, the refractive index varies smoothly in the $z-$direction and therefore $g(z)$ traces the compositional gradient. For rough interfaces there are discontinuous changes in refractive index at the interface boundaries and $g(z)$ is accounted by normalizing height distributions. The averaging aspect of the "interface width" concept is clear from Fig. 2-6, where two different interface structures. i.e., a chemically intermixed and a physically rough interface resulted in an identical $g(z)$, $f(z)$, and hence also similar σ. An obvious disadvantage of using this formalism for roughness analysis is therefore, the lack of discrimination between intermixing and roughness for multilayer structures constituting mixed profiles.
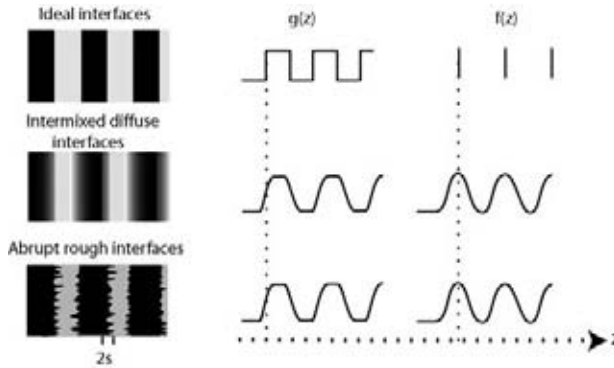
Figure 2-6: One dimensional interface profile function $g(z)$ and its spatial derivative $f(z)$ for ideal, intermixed, and rough interfaces. The notable is the same interface width σ of the two later kinds.

In most cases, the overall shape of the deviation from an ideal interface is taken into account as a Gaussian distribution and is accounted by "Debye-Waller" factor which incorporates average interface width as "r.m.s roughness, σ," into the multilayer reflectivity theory as,

$$R = R_o \exp(-\frac{4\pi\sigma\sin\theta}{m\lambda})^2 \tag{2.14}$$

where,
R =absolute reflectivity
R_o = theoretical reflectance for an ideal interface
σ = average interface width
θ = grazing incidence angle
λ = X-ray wavelength

m = order of Bragg reflection

The exponential dependence of absolute reflectivity, R, on σ^2 for a single interface is clearly more dominant for shorter soft X-ray wavelengths or shorter multilayer periods and/or higher incidence angles (Eq. 2.1). This is illustrated in Fig. 2-7 (a), showing simulations of reflectivities ($\theta = 90°$) versus interface width, at three wavelengths ($\lambda = 13.4, 3.11, 2.74$ nm) for three multilayers (designed at the corresponding wavelengths). A larger impact of interface widths at larger angles is depicted in Fig. 2-7 (b) for the shortest λ (for a Cr/Ti multilayers). It is clear that, both, shorter wavelength and higher angle X-ray reflections require multilayers with extremely small periods and in order to have minimum ratio of σ/Λ (Eq. 2.14) the interface width, σ , if not completely eliminated, should be as small as possible.
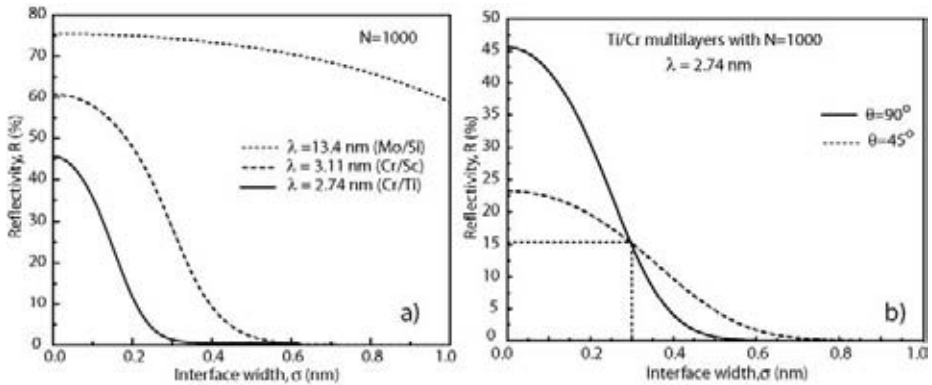

Figure 2-7: Simulations: (a) showing normal-incidence reflectivity dependence on interface widths, for Mo/Si, Cr/Sc, and Cr/Ti multilayers. It is illustrated that σ is more dominant at shorter wavelengths, i.e., for thin multilayers. Multilayer materials at each wavelength are chosen according to the above described criterion, and (b) showing $R(\sigma)$ profiles of Cr/Ti multilayers, at normal incidence, $\theta = 90°$, and Brewster angle, $\theta = 45°$.

The surface height fluctuations (Fig. 2-6), if not completely uncorrelated, can be further classified on the basis of lateral, $\xi_{\parallel}$, and vertical, $\xi_{\perp}$, roughness parameters called correlation lengths. These are the characteristic length scales: between lateral repetition of roughness features, and vertical extent up to which roughness reproduce its initial occurrence. As shown in Fig. 2-8 for a single interface a surfaces associated with a shorter $\xi_{\parallel}$ (compared to the X-ray wavelength) will be more "jagged"(a), while longer $\xi_{\parallel}$ (also termed as low spatial frequency roughness) correspond to locally smooth but "wavy" surfaces (b). A combination of these two (c) actually needs an extra parameter, α, which provides a measure of short range ($< \xi_{\parallel}$) surface roughness embedded in $\xi_{\parallel}$.

Associated with a multilayer having many consecutive interfaces, are other kinds of roughnesses. As already described the roughness progression correlated perpendicular to the interfaces is described by $\xi_{\perp}$. For almost all multilayer systems the overall roughness increases with increasing number of bilayers or the total thickness of the stack and is called accumulating roughness. From the multilayer X-ray reflectivity point of view accumulation of the lateral
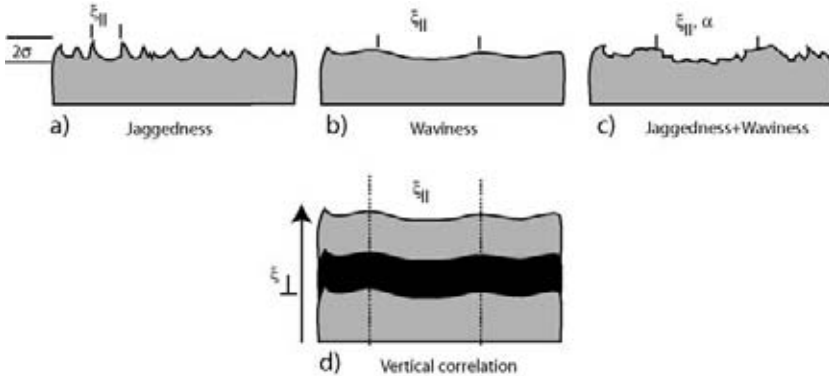
Figure 2-8: (a) High, (b) low, and (c) mixed spatial frequency roughnesses for single interfaces, all having similar average interface height fluctuations of 2σ. $\xi_{\shortparallel}$ indicates the lateral coherence length, while α measures short range disorder within $\xi_{\shortparallel}$. d) $\xi_{\perp}$ is a measure of the vertical roughness correlation length for a multilayer.

roughness $(\xi_{\shortparallel}, \alpha)$ will increase the diffusely scattered intensity around the specular beam, and the correlation length will effect the angular distribution of the incoherent halo around the specular direction [24], [25], [26]. On the other hand, vertically correlated roughness will behave like an ordered structure and reflectivity will distribute into sheath where the Bragg condition is fulfilled. One should keep in mind during roughness interpretation that the reflective features of a multilayer with correlated interfacial roughness change non-linearly with the operating wavelengths of the mirror and the correlation length scales are all relative[1].

A quantitative evaluation of the roughness parameters requires an extensive theoretical research and has therefore only been qualitatively studied during this work. Varying roughnesses associated with different material systems, used in this work are discussed in Chapter 5.

---

[1]But how smooth is smooth enough?   *D.G.Stearns* [22]

Chapter 3

Multilayer Growth

Theoretical and experimental aspects of sub-nm multilayer growth under the influence of low-energy ion-bombardment are treated in this chapter. Prospects of interface quality improvement by implementing a novel technique of modulated ion assistance are discusssed with some examples from the present work.

It has been known for a while now that during sputtering low-energy (25 to 100 eV) ion bombardment alters growth kinetics and promotes low defect densities and smooth interfaces [27], [28], and therefore multilayer mirrors in this work were fabricated by sputter deposition technique. The fundamental species involved in sputtering of atoms from a solid target by energetic ion bombardment are schematically shown in Fig. 3-1. The number of atoms removed and the secondary electrons emitted per incident ion are expressed as the sputtering yield, S, and the secondary electron yield, γ, respectively. Both quantities depend on target material and the bombarding species which, in most cases, are sputtering gas ions from the surrounding plasma. Sputtered atoms are ejected in knock-on collisions and form a film upon condensation on any available surface, for instance a substrate. The energies of the atoms arriving the substrate are normally a few eV, which is not sufficient to provide enough surface mobility to grow smooth layers. Fortunately, the surface mobility can be enhanced if positive ions from the working gas, extracted from the plasma, are accelerated towards the surface of the growing film, thus altering the growth kinetics and resultant microstructures. A confinement of secondary electrons by magnetic fields close to the magnetron, enhances the ionization and hence the sputtering probability. Magnetic fields also provide a way of guiding the ions to the growing surfaces. Sputtering gas neutrals reflected from the target surface constitute dominant energetic species. Their energies depend on e.g., the relative masses of the target and sputtering gas atoms and the incoming ion energies. These neutrals can be used as an alternative for ion-bombardment, especially, where magnetic confinement or ion guidance can not be achieved. Before going into the details of experiments and physical aspects of multilayer formation, a theoretical model to calculate the required range of ion energies and fluxes for multilayer growth is presented in the next section.

3.1 Ion-surface Interactions

Several elastic and inelastic processes are involved in momentum and energy transfer, during ion-bombardment of the growth surface through nuclear and/or electronic interactions. One of the physical processes for energy transfer from ions is through kinetic displacements of the
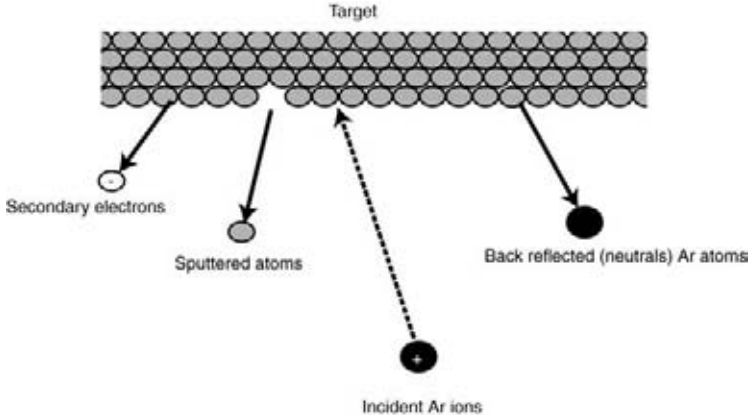
Figure 3-1: A schematic of the sputtering process at the target surface by Ar ions. Fundamental species involved in the momentum and energy transfer are marked in the figure.

surface or bulk atoms of the growing layers. An estimate of the ion-energy range required to cause surface atom displacements, in order to provide sufficient ad-atom surface mobility while avoiding bulk damage, can be useful in selecting process conditions for soft X-ray multilayer mirrors. For such calculations, the input parameters are energy of the bombarding ions, E surface, $E_d^{(s)}$ and bulk $E_d^{(b)}$ displacement energies of the underlying film, masses of the ion and surface atoms, and angles of impact. Considering these, a theoretical model based on a binary collision approximation [1] is used to estimate the appropriate ion-energy range prior to multilayer deposition with any new material combination. In the calculations it is assumed that the cohesive energy of the underlying lattice (closed pack structure) is a direct measure of the bulk displacement energy, $E_d^{(b)}$, and, owing to fewer chemical bonds and hence weaker bonding strengths the surface displacement energies are assumed to be half of the bulk displacement energies i.e. $E_d^{(s)}=1/2 E_d^{(b)}$.

Though a simplified approach, this model has proven consistence with experimental results in several cases [*Paper I, II, and VII, in this thesis*]. For example, the deposited energy per ion to cause lattice (surface/bulk) displacements by Ar ion impingement on the growing surfaces of Ti and Cr are calculated versus the initial ion energy from $0 - 100$ eV. As shown in Fig. 3-2 at very low ion energies < 21 eV no surface displacements are expected, while ion energies between about 21 eV to 51 eV are more likely to cause displacements 'primarily' on the surface or about a monolayer (ML) below the surface layer. Ion energies higher than 51 eV would cause both surface and bulk (> 1 ML) displacements for this material system. A validation of calculated energy range ($20 - 50$ eV), the so called allowed *energy-window,* was experimentally tested and the ion-energy optimization to obtain smooth layers (described in a later section) resulted in 21.2 eV and 23.7 eV for Cr and Ti, respectively, which are energies just within the surface displacement region.

Another outcome of the calculations is the required ion-fluxes to cause surface displacements within the energy window. The two horizontal lines in Fig. 3-2 at 13.42 and 11.27 eV indicate $E_d^{(s)}$ of Ti and Cr lattices, respectively. An ion with initial energy of 25 eV will impart
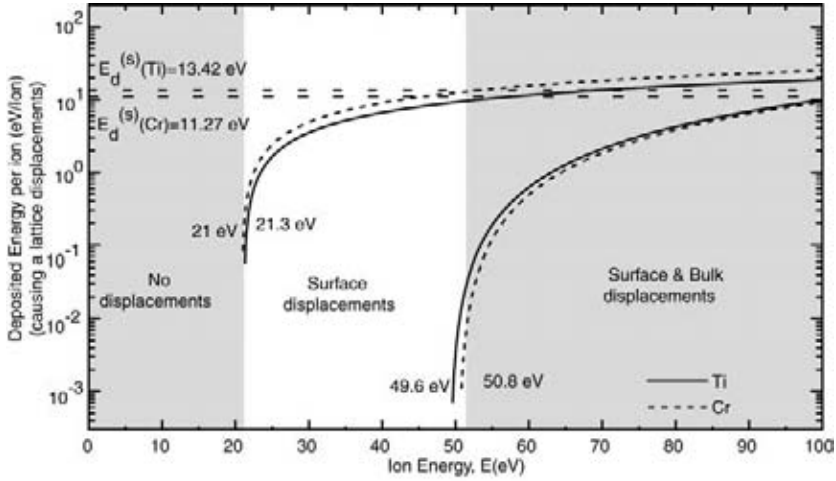
Figure 3-2: Surface and bulk displacements energy profile for Ti and Cr lattices.

a fraction of about 2 eV to lattice displacements, therefore a relatively large number of ions i.e. a high ion-to-metal flux ratio $\Phi(J_{ion}/J_{met}) \backsim 6$ is needed to assist growth of Cr/Ti multilayers at these low energies. For this we applied a solenoid around substrate position to guide the secondary electrons through magnetic field lines resulting in high ionization and hence high Φ values closer to the growing films, as is described in the next section.

3.2 Experimental Details

A dual-cathode DC magnetron sputter deposition system with a chamber size of 500 mm diameter, 350 mm in height, and a target-to-substrate distance of 120 mm has been used to deposit all multilayers [29], [30]. The system is equipped with two circular magnetron sources having unbalanced type-II magnetic configuration with opposite polarities. As shown in Fig. 3-3 the two magnetrons, of 75 mm diameter, are mounted at off-axis positions with a tilt angle of $25°$ to the substrate normal. An electrically isolated μ-metal shield between the magnetrons serves to protect the targets from cross-contamination, and also to push the magnetic field lines closer towards the substrate. This configuration leads to strong magnetic fields from the outer poles extending into the chamber where they couple to a separate solenoid surrounding the substrate. The solenoid consists of 220 turns of capton insulated Cu wire ($\phi = 2$ mm) wound on a stainless–steel frame with an inner diameter of 125 mm. The target materials used were 99.9% pure in all cases and the target discharges were established with constant-current power supplies and discharge currents (voltages) of about 0.06 A (-300 V) were used. This yielded deposition rates of about $0.01 - 0.05$ nm/s. Both magnetrons were running continuously during the deposition. The material fluxes to the substrate were regulated by fast acting computer controlled shutters located in front of the magnetrons. All depositions for the current work were carried out using chemically cleaned Si(001) substrates mounted on the electrically isolated

substrate table, rotating at a constant rate of 60 rpm. A negative potential between 0 and 50 V was applied to the substrate during the deposition. The background pressure prior to deposition was about 2×10^{-7} Torr and a low pressure of about 3 mTorr Ar (99.999% purity) gas was maintained during the depositions. The deposition rate of each material was determined by growing two multilayers with known deposition times, but with different layer thickness ratios, Γ. The multilayer periods were then calculated from the positions of the multilayer peaks in low-angle hard X-ray reflectivity patterns. This yield an equation system from which the individual deposition rates can be extracted [31].
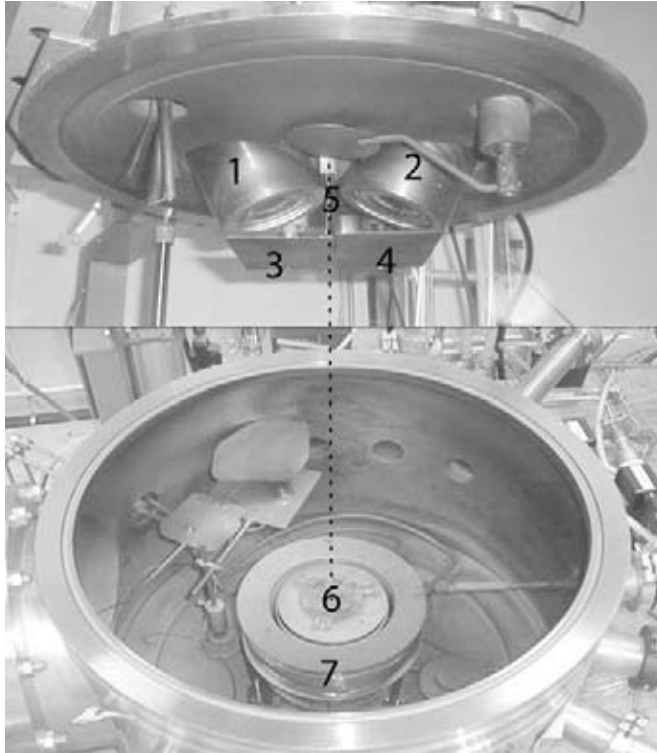
Figure 3-3: An overview of the deposition chamber: Marked components are the magnetrons (1,2), the fast acting shutters (3,4), the isolation shield between the magnetrons (5), the rotating substrate holder (6) and the solenoid (7) surrounding the substrate table.

Either no magnetic coupling or a solenoid current of 5 A (with a direction that couples the magnetic field of the solenoid to that of the magnetron being used for deposition), was used to obtain two different field line configurations, shown in Fig. 3-4. The magnetron-solenoid coupling configures the magnetic field lines and can indirectly be seen by the plasma glow (due to ion-electron recombination in high ionization regions) inside the chamber. Fig. 3-4 (a) depicts a situation where the solenoid is turned off (0 A) and the ionization takes place

predominantly near the targets, leading to $\Phi < 1$ at the substrate. Turning on 5 A current in the appropriate direction couples the solenoid to either the left Fig. 3-4 (b) or the right Fig. 3-4 (c) magnetron. It can be concluded by ocular inspection of the plasma paths that the magnetic field lines guide the secondary electrons (generated in the sputtering process) from the magnetrons all the way down to the substrate resulting in a significant enhancement of the ionization of the working gas ($\Phi > 1$) in the vicinity of the growing film. This enhanced ion-density, as explained earlier, plays a central role in providing the required surface energy in order to engineer smooth and abrupt interfaces between growing layers. The negative bias applied to the substrate was used to attract this high flux of ions from the surrounding plasma to the growing film with definite kinetic energies. Absolute values of the ion-energies and ion-to-metal flux ratios, Φ, were determined by plasma probe measurements, as described in the next section.
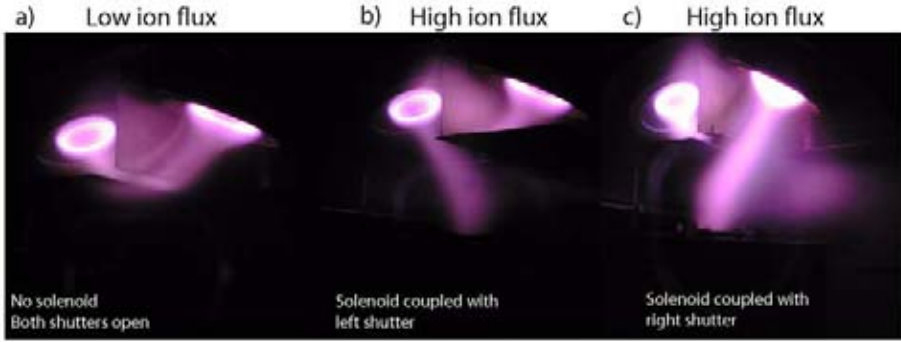

Figure 3-4: Three type of magnetic field configurations inside the deposition chamber generated by: (a) without solenoid coupling, (b) left magnetron is coupled with the solenoid, and (c) right megnetron is coupled with the solenoid.

3.2.1 Plasma Characteristics

The plasma under discussion is a low pressure non-equilibrium discharge, having a low degree of ionization of 10^{-2}, and a charged particle density i.e., electron density (n_e) $\cong$ ion density (n_e) of about 10^{-9} cm^{-3}. In spite of the equivalent charge densities, electrons mobilities are at least 100 times higher than ions normally, resulting in a small positive potential buildup in the plasma, V_p. Another consequence of high electron velocities is the formation of a charge depleted region, the so-called "*dark space*", close to any surface facing the plasma. For a typical magnetron plasma at low pressure < 10 mTorr, and substrate bias voltages, V_s, down to 150 V the thickness of the dark space is on the order of a few mm. As previously mentioned, the ion energy, E_{ion}, and the ion-to-metal atom flux-ratio $\Phi(J_{ion}/J_{met})$, are the primary parameters controlling adatom mobilities on the growing film. In order to relate V_s to E_{ion} it is necessary to know the plasma potential, V_p, at the dark space edge, from where the ions are accelerated towards substrate. If the pressure is sufficiently low, such that the mean-free path for ions is longer than the dark sheath length, E_{ion} can be expressed as,

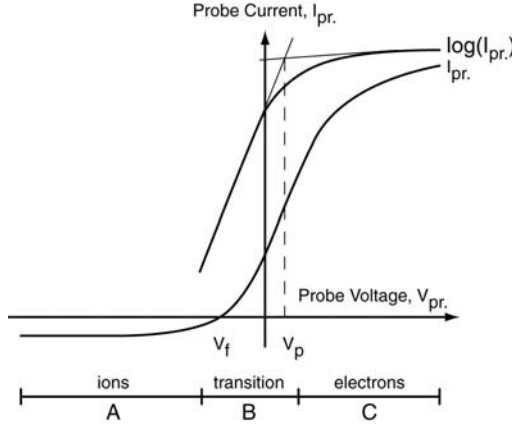$$E_{ion} = nq \mid V_s - V_p \mid , \tag{3.1}$$

Figure 3-5: Typical current-voltage characteristic curve obtained by a Langmuir electrical probe. Three regions of interest are marked with A, B and C.

where n is the valency, and q is the charge of the ion. All these parameters depend on the geometry, chemistry and electromagnetic field configuration in the discharge. For most metal targets considered in this work E_{ion} varies from 0 to 50 eV.

In order to characterize the sputtering plasma, I-V curves (Fig. 3-5) measured by electrical probes, placed at the sample position, were used. In such measurements the total probe current, I_{pr}, is measured versus the total applied probe voltage, V_{pr} [32].

I_{pr} is the sum of electron and ion-currents, I_e and I_{ion} respectively. The potential where the electronic and ionic contribution to I_{pr} are equal (i.e. $I_{pr} = 0$) is called the floating potential V_f which is the potential attained by the electrically isolated sample. A typical plasma probe I-V curve, as shown in the Fig. 3-5, has three different regions on the basis of V_p and V_f.

A. Region A is the ion-saturation region where electrons are repelled by the probe. To determine the ion current density a flat probe of stainless-steel is used. The probe is surrounded by a stainless-steel shield with the same potential as the probe in order to prevent edge effects to influence the effective collecting probe area.

B. In the transition region B, an ion current is collected by the probe and electrons with kinetic energy larger than (V_{pr}-V_p) will also reach the probe and contribute to I_{pr}. A *Langmuir probe,* a few mm long tungsten wire, is used to determine the plasma potential in this region, as well as in region A. The plasma potential can then be determined by plotting $\log(I_{pr})$ versus V_{pr} by the crossings of the tangents of the slopes in the transition region B and in the electron saturation region A, see Fig. 3-5.

C. C is the electron-current region, where the probe potential is higher than V_p, and therefore, ions are repelled by the probe and I_{pr} is governed by I_e.

An Ar sputtering pressure of about ∼3 mTorr implies about an order of magnitude longer mean free path for ions than the dark sheath. Hence, the probability of collision in the dark space is very low and, for decreasing voltages to the probe no electrons reach the probe,

only positive ions are collected. The measured current, I_{ion}, can be used to calculate the ion flux J_{ion}, i.e. the ion current drawn through the sample divided by electron charge,e, and A (the area of the probe) according to:

$$J_{ion} = \frac{I_{ion}}{Ae}.$$ (3.2)

Using the deposition rate, r, the density of the film, ρ, and the molar mass, M, of the metal atoms, the flux of metal atoms, J_{met}, can be determined by,

$$J_{met} = \frac{N_{met}}{At} = \frac{\rho N_A r}{M}.$$ (3.3)

By these two equations, the ion-to-metal flux ratio, Φ, can be calculated as,

$$\Phi = \frac{J_{ion}}{J_{met}} = \frac{I_{ion}M}{\rho N_A r Ae}.$$ (3.4)

3.3   Interface Engineering by Ion-energy Modulation

As compared to a low flux, high ion energy bombardment the use of high-flux bombardment with low energy ions results in homogeneous multilayers with considerably flatter interfaces. Nevertheless, the energy of the ions for surface displacement is chosen at the cost of some surface damage which leads to intermixing at the boundaries of two materials for these sub-nm scaled multilayer's interfaces. In order to get improvement in abruptness the research, at this point, has been further elaborated by the idea of using a two-stage growth mode of each individual layer, so called "modulated ion-assistance", in order to obtain flat and chemically abrupt interfaces. Theoretically, the concept has been shown to be promising by molecular dynamics simulations for two-stage low-energy ion assistance growth of, Ni/Cu/Ni layers [33].

A growth optimization of Cr/Ti multilayer system is taken as an example here to elaborate the modulated ion-assistance. The plasma potentials, determined from the Langmuir probe measurements, for deposition of these two materials were V_p(Ti) = 1.7 V and V_p(Cr) = −1.3 V, respectively. The negative plasma potential for Cr could be a result of high flux of secondary electrons magnetically guided from the Cr target. The ion-to-neutral flux ratios were calculated to $\Phi_{Ti} = 3.3$ and $\Phi_{Cr} = 2.2$, respectively.

The ion-potential (energies) involved at each stage of Ti and Cr layer growth are shown in Fig. 3-6. The first 0.3 nm of each Ti and Cr layer were grown without ion assistance (i.e., substrate was held at 0 V) which resulted (Eq. 3.1) in E_{ion}(Ti) = 1.7 eV, and $E_{elec.}$(Cr) = 1.3 eV. Practically, these low ion and electron energies have insignificant impact on the growth kinetics and at room temperature deposited atoms will stick on the surface without any displacements. The resulting layer will then be porous and rough, but the probability of interdiffusion with the underlying layer is expected to be minimal. The remaining $0.39 - 0.72$ nm layer thicknesses were then grown with relatively high ion energies ($E_{Ti} = 23.7$ eV and $E_{Cr} = 21.2$ eV), which are in the range of the calculated energy window for sufficient surface displacements (Fig. 3-2). The intention of increasing the ion energies were to densify the layers and smoothly terminate the surfaces before the onset of the next layer in a multilayer sequence.

Although an indirect way of assessment, the experimental success of increased interface quality by modulated ion-assistance is evident from Fig. 3-7, where the first order Bragg peak in the hard X-ray reflectivity scans is compared for three different Cr/Ti multilayers, each containing 20 bilayers. Fig. 3-7 a), contains the reflectivity curves for the multilayers grown with a continuous ion assistance. The multilayer grown under kinetically restricted conditions with $E_{ion} = 1.5$ eV, shows a much lower reflectance than the multilayer grown with low energy
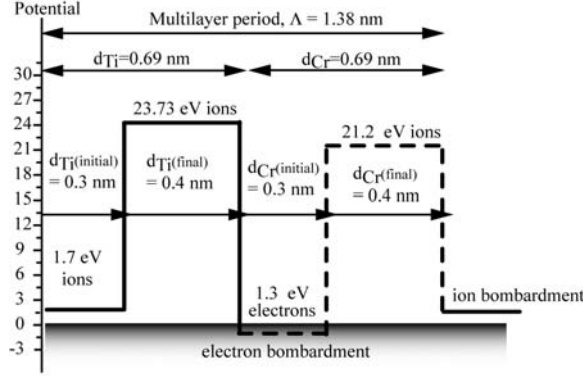
Figure 3-6: Potential (ion energy) vs. growth diagram for a single bilayer of a Cr/Ti ML with a modulation period of 1.38 nm. Initial, d(initial), and final, d(final), thicknesses of individual Ti and Cr layers are labelled together with ion energies in the corresponding regions. All numbers written in the figure represent the optimised values, based on the comparison of low-angle hard X-ray reflectivity for several different Cr/Ti multilayers containing 20 bilayers.

ion-bombardment of $E_{ion} = 22$ eV. Furthermore, the multilayer grown by ion-energy modulation according to optimized parameters (Fig. 3-6), is compared in Fig. 3-7 b), which resulted in a significant increase in reflectance. A more thorough discussion of interface roughness reduction by implementing modulated ion assistance in different materials systems is included in Chapter 5.

3.4 Multilayer Formation During Low-energy Ion Bombardment

In general, film growth under highly non-equilibrium processes like sputtering is a combined effect of adsorption and diffusion of energetic species as they condense from the vapor phase onto a cold substrate. The number of sputtered species sticking to the substrate depends on substrate temperature, deposition rates, impurity concentrations, and the surface energies. Unfortunately, the exact spatial and temporal distribution of surface atoms during metal multilayer growth, concurrent with energy transfer by ion bombardment, is not a well-understood area.

The three most general representations of film formations are schematically shown in the figure Fig. 3-8. The parameters γ_A, γ_B, are the film and substrate surface energies, respectively, and γ_i is the film-substrate interface energy.

The contact angle, φ, is determined by the growth process and the relations of the surface/interface energies as:

$\gamma_B < \gamma_A + \gamma_i$ gives $\varphi > 0$ (island growth)
$\gamma_B > \gamma_A + \gamma_i$ gives $\varphi \simeq 0$ (layer-by-layer growth)

It is usually considered in the optical community that growth of metal-on-metal or metal- on-semiconductor begins either by direct island formation or establish into islands after
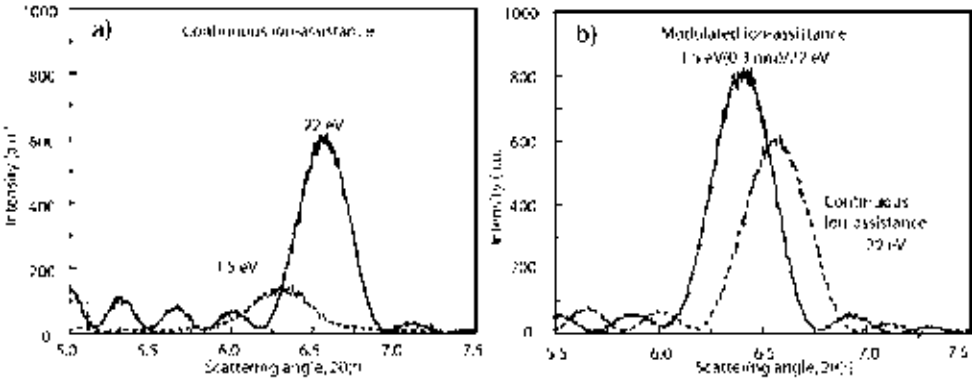
Figure 3-7: Hard X-ray reflectivity scans around the first order Bragg peak for three multilayers each with N= 20. a) multilayers grown with continuous ion-assistance, b) comparison between best obtained multilyer with continuous ion-assistance and modulated ion-assistance.
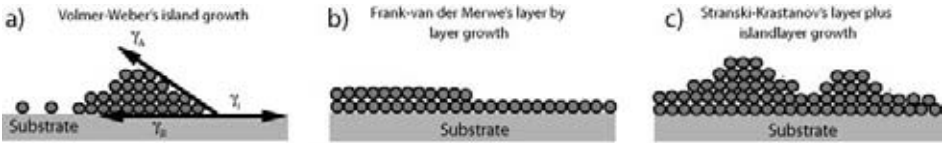
Figure 3-8: Schematic representation of the three most known growth modes during the initial stage of layer formation: a) Volmer-Weber's island formation, b) Frank-van der Merwe's layer-by layer growth and, c) a combination of the first two modes is Stranski-Krastanov's layer plus island growth.

few monolayers i.e., Stranski-Krastanov's growth mode. This is mainly due to the stronger interactions in-between the metal atoms than the film-substrate interaction [34], [35]. The growth initiates with 3D island formation which turns into a continuos film upon coalescence of these islands at some threshold thickness. The mean threshold thicknesses are, normally, 1-20 nm for most metals. In practice, fabrication of normal-incidence soft X-ray mirrors demands individual layer thicknesses normally not more than 2 nm and thus island growth would result in a low density, porous, films. Moreover, in multilayers atoms arrange themselves on one (similar) or another (dissimilar) material in short sequences, which cannot be compared to single metal film grown on a substrate. Furthermore, the high density of interfaces actually change the layer morphology compared to bulk structures by affecting re-nucleation and dislocations distribution. Nevertheless, the ion bombardment, with appropriate ion-energies and fluxes, is indispensable for structuring metal multilayers formation for extremely thin multilayers as it can:

- Continuously re-dissociate already nucleated islands, if any, hence favoring the quenching of ad-atoms into 2D layers. As a consequence, porosity can be overcome in thin layers and, theoretically, it is possible to grow complete layers as thin as 0.3 nm.

- Transfer sufficient energy to enhance surface mobility and ad-atom diffusivity in order to trigger the atomic arrangement into smooth layers. This, in addition to layer densification, terminate the surfaces without any irregularities and hence smooth interfaces can be realized.
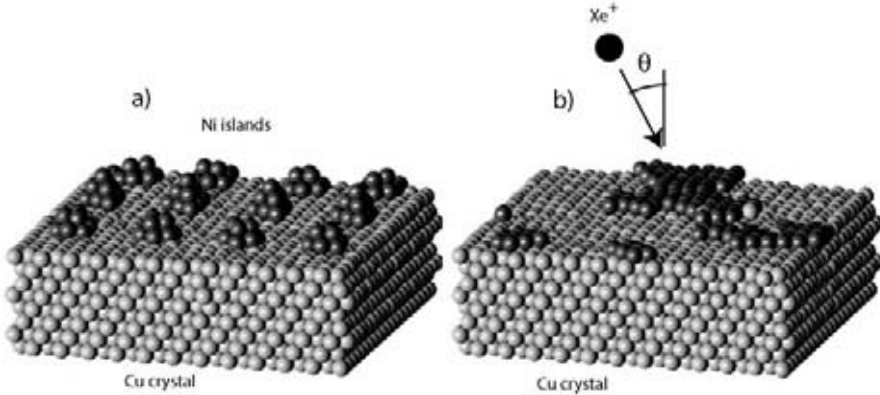
Figure 3-9: Molecular dynamics simulations done by Zhou *et al.*[36], shows the Ni islands (formed on Cu crystal) dissociation by 12 eV Xe ions within impact angles of $\theta = 0 - 70°$.

The potential of ion assisted multilayer growth has also been reported in a theoretical work done by Zhou *et al* [36]. They showed by using molecular dynamics simulations of Ni/Cu multilayer (Fig. 3-9) growth concurrent with Xe ion assistance, that Xe ions with 12 eV ion energy are beneficial to rupture the Ni island nucleation when ion impingement angles are within $0 - 70°$. It has also been shown by calculations that there is an optimum ion energy and impact angle where maximum flattening of the layers with minimum intermixing can be achieved.

The ion-energy required to promote smoother growth may also induce some unavoidable damages like: re-sputtering of deposited material, ion-implantation and bulk diffusion or intermixing at the onset of each layer formation. In one of the previous example [Fig. 3-7 (b)], the lower reflectivity obtained for the sample grown with a homogeneous ion energy of 22 eV is believed to be caused by ion- induced intermixing. It has also been realized that the ion-energy modulation of individual layers is more beneficial when amorphous layers are concerned. Fortunately, sputtering of metals is more likely to promote an amorphous layer structure as long as individual layer thicknesses are below some critical limit for crystallization (above the limit the amorphous layers often convert into polycrystalline layers). The surface roughness that arises with the growth of crystallites could be overcome by high initial ion energies > 100 eV but, at the cost of a large intermixing.

Chapter 4

Multilayer Characterization

> *There is no single technique which can look into hundreds of interfaces buried within sub-nm thin layers and give comprehensive compositional and structural information. However, multilayer investigation by a combination of characterization probes has shown to be useful in exploring these structures.*

Comprehensive structural analyses of multilayers were performed by hard X-ray reflectivity and diffraction measurements complemented with high resolution cross-sectional transmission electron microscopy and electron diffraction. Since the studies were partially focused on *the role of impurities in defining a multilayer structure,* compositional determination of the multilayers grown with and without intentional incorporation of impurities were made by ion beam analyses. The thermal stability of the multilayers was investigated by *in situ* annealing during hard X-ray reflectivity measurements and *ex-situ* scanning transmission electron microscopy and simultaneous energy dispersive X-ray spectroscopy. For selected multilayers, mirror performance was investigated using soft X-ray wavelengths. According to the nature of the characterization probes i.e., X-rays, electrons, and ions the discussion here is divided into : X-ray reflectivity, electron microscopy and ion beam analyses. The aim of this chapter is to provide an introduction to the experimental techniques and to discuss the information obtained pertaining to the multilayer structures.

4.1 X-ray Analyses

4.1.1 Hard X-ray Reflectivity

Characterization of multilayer coatings by hard X-ray reflectivity (HXR) (is certainly the most natural routine and therefore) was made on every single sample taken out of the deposition chamber. Reflection of X-rays in multilayers under grazing incidence generate a characteristic interference pattern which, in conjunction with simulations, can be used to analyze the multilayer structural parameters. For this work, an in-house diffractometer *Philips X'Pert-MRD* with copper source (Cu K_{α}, λ=0.154 nm) operating at 0.8 kW was used. The diffractometer has de-coupled detector (2θ) and sample (ω) axes. Out of several different combinations of primary (between the X-ray tube and the sample) and secondary (between the sample and the detector) optics, parallel beam (Thin film) optics were found to be the best suited for reflectivity analysis of deposited multilayers. The parallel beam optical configuration was achieved by having the x-ray line source, Ni- β filter (to suppress K_{β} radiation), and a fixed divergence slit of $1/32°$ in the primary path, whereas the detection angle in the secondary path was defined by selecting the central channel of a $0.3°$ parallel plate collimator followed by a flat graphite
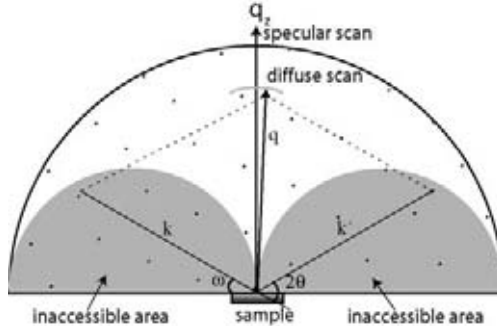
Figure 4-1: A reciprocal space representation of a typical X-ray scattering experiment. The incident X-rays with a wave vector k are scattered at an angle 2θ, and changed into a reflected wave vector, k'. The scanning in radial or transverse direction of resultant vector q provides an in depth or lateral scattering information, respectively. The gray areas are inaccessible according to the X-ray scattering geometry.

crystal monochromator. A proportional detector (PW1711/96 with 500 kcps maximum count rate) was used for data acquisition. As a complement, a Philips powder diffractometer with a line-focused copper anode source, operating at 0.8 kW, and a proportional detector was also used in low angle ($0° - 15°$) reflection geometry and for standard high angle x-ray diffraction (XRD). In this equipment a Ni $\beta-$filter, a $1/4°$ divergence slit, and a 2 mm brass mask were used for the primary optics and a 0.1 mm anti-scatter slit, a $1/4°$ divergence slit, matched to that on the primary side, followed by a bent Ge monochromator, was used as secondary optics.

Depending on the source-sample-detector coupling, two types of one-dimensional scans: specular reflectivity and diffuse scattering measurements were made in this work. Specular scans, so called $\omega - 2\theta$ scans, were made by maintaining the detector angle (2θ) twice the incidence angle on the sample ($\omega = \theta$) during the scans. In this configuration, as illustrated in Fig. 4-1, the resultant reciprocal scattering vector, $q = k - k'$ is always along the surface normal, q_z, and its magnitude is a function of angle, θ, as

$$| q | = \frac{4\pi}{\lambda} \sin \theta. \tag{4.1}$$

X-rays in $\omega - 2\theta$ scans thus probe the chemical modulation sequence of the multilayers in the growth direction. A typical reflectivity curve obtained in such a scan is shown in Fig. 4-2 (a) for a Cr/Sc multilayer containing 100 bilayers. The peaks, labelled m=1, 2, and 3, are the first three orders of Bragg reflections, originating from the multilayer periodicity Λ, and can be used to determine the multilayer period using Eq. 2.5. However, since according to Porods Law [15] of surface scattering X-ray intensity ideally goes down as $1/q^4$ (for all materials) and presence of rough surfaces and interface imperfections account even a faster drop, higher order reflections are difficult to get for short period multilayers using lab X-ray sources. For example Ni/V multilayers, which are required as X-ray mirrors to operate at λ=2.43 nm, have multilayer periodicities as small as 1.2 nm and the first order multilayer peak does not appear until 2θ becomes $7°$ where a very low intensity remains. Further reduction in reflectivity from Ni/V multilayers occur due to considerably high interface distortions. Nevertheless,
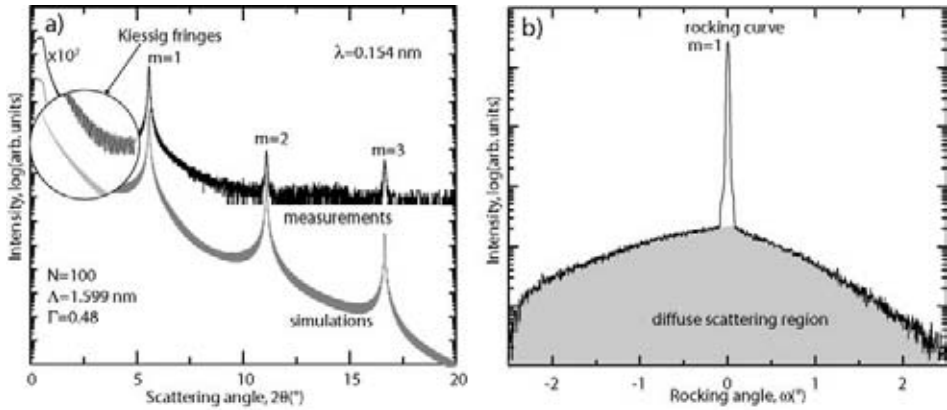
Figure 4-2: (a) Cu-K$_\alpha$ reflectivity measurements for a Cr/Sc multilayer containing 100 bilayers. The peaks in the reflectivity curve corresponds to the first three multilayer Bragg reflection.The simulation (lower curve) yielded modulation period of Λ=1.599 nm and Γ=0.48, (b) Rocking curve scan around m=1. Gray area represent the diffusely scattered X-ray intensity, while enhancement in specular reflectivity appears in peak direction.

since $\bar{\eta} \approx 1$ the refraction effects could safely be neglected at these angles and the multilayer period was determined by considering only one reflection. Moreover, with the availability of compatible computational tools [20] simulations [lower curve in Fig. 4-2 (a)] were made, mainly to determine the multilayer period and individual layer thicknesses.

Another peculiar feature of low angle reflectivity curves is the sequential interference of X-rays from the surface and the film/substrate interface, known as *Kiessig fringes* [37]. Due to finite thickness of the multilayer being a multiple of Λ, theoretically N-2 distinct destructive interference minima, in-between two consecutive Bragg reflections, are expected. The visibility of Kiessig fringes was used as a qualitative layer conformity measure when different multilayers were compared in this work.

Additionally, ω rocking scans were performed to measure the diffusely scattered intensity in non-specular directions. As illustrated in Fig. 4-1, varying ω allows to explore different directions of the scattering vector around a Bragg peak, while keeping its magnitude constant. Scattered intensity around the Bragg peak appears as a shoulder in the background (see shaded region in Fig. 4-2 (b). The diffuse-to-specular integrated intensity ratio provides a qualitative measure of the overall lateral roughness in a multilayer structure.

At this point, a few potential ambiguities in determining the detailed structural roughnesses of the multilayers through comparison between experiment and model simulations should be mentioned. One has to include the associated roughnesses, thicknesses and densities of Si-substrates, and the native SiO$_2$ layer top layer oxidation. These parameters mostly influence the shape of the reflectivity curve and do not alter the peak positions or their relative intensities. The assumption of nominal bulk densities for the multilayer constituents and impurity-free layers influence the critical angle as well as the relative intensities of the Bragg peaks, when computing the reflectivity multilayers. Two strongly competing parameters which influence the relative intensities as well as the peak appearance are the structural parameter of thickness

ratio, Γ, and the asymmetric interface widths, σ, of the multilayers. For instance; according to the interference theory, a complete destructive interference should occur for second order Bragg reflection when $\Gamma=0.5$. However, second order reflection is often visible, which can be accounted for either by iterating the Γ or by assigning asymmetric interface widths in the multilayer structure. The multitude of iterative parameters for several hundred interfaces complicates the interpretation of the computed results and thus, it is not straightforward to fit the roughness parameters from $\omega-2\theta$ HXR curves containing less than three orders of Bragg peaks. Unfortunately, in spite of extensive efforts, comprehensive modelling of rocking-curves proved even more difficult than specular reflectivity analysis and is not suitable for routine sample analysis, [22]-[24].

During this work, the IMD simulations for HXR analysis were mainly used for multilayer period determination, while a quality measure of the multilayers was made by comparison between multilayers with similar structural parameters for Bragg peak intensities, visibility of Kiessig fringes, and diffuse-to-specular integrated intensity ratios.

4.1.2   X-Ray Diffraction

Most of the multilayers in this work are comprised of *X-ray amorphous* layers and, therefore, X-ray diffraction (XRD) which provided useful information regarding the structure of some supperlattices and multilayers containing thicker polycrystalline or nanocrystalline layers, was not routinely used. XRD is conceptually similar to XRR, probing higher θ values in conventional θ-2θ scans (see. Fig. 4-1). As a corollary, small periodicities regarding atomic arrangements in the planes perpendicular to the scattering planes could be obtained. Additionally, a measure of the average size of the grains can also be determined by measuring the FWHM of the corresponding Bragg peak [38].

Occasionally, pole figures were also recorded by rotating the azimuth angle (ϕ) and polar angle (ψ) whilst keeping 2θ at selected Bragg reflections, to obtain information regarding orientation of the crystallites. A set of pole figures measured for Cr (002) reflection (at $2\theta = 64.58°$) are shown in Fig. 4-3 for the three Cr/Sc multilayers investigated for the effects of ion energetics, as presented in *Paper II* (Fig.3-a). The central $(\psi, \phi) = (0, 0)$ double reflection in all three figures stems from 2θ -overlap with a substrate peak. It can be seen that the multilayers grown with ion assistance exhibit a pronounced symmetric reflection ring at $\psi \simeq 45°$, corresponding to a homogeneous ϕ-distribution of Cr (002) planes which means that the preferred orientation of Cr crystallites is (110). In comparison the multilayer grown without ion assistance exhibit a weak ring at this tilt angle. This analysis shows that ion assisted growth promotes a fiber texture of Cr crystallites compared to almost randomly oriented crystallites in the multilayer grown without ion assistance.

4.1.3   Soft X-ray Reflectivity

Soft X-ray reflectivity (SXR) is the ultimate characterization technique to test the multilayer performance and was used for selected multilayers; specifically designed as near-normal incidence mirrors and as analyzers for polarized synchrotron radiation. Due to a large required spectrum of EUV and soft X-ray wavelengths region, the use of synchrotron radiation was indispensable. The main benefit of course, in addition to higher X-ray intensity, is the reflectivity measurement both as a function of energy and angle. Measurements took place at two synchrotron sources: *BESSY (Germany)* and *ALS (USA)*. At BESSY, a triple-axis UHV reflectometer/diffractometer connected to the exit slit of the beamline *UE56/1-PGM,* based on an elliptical undulator coupled with a plane grating monochromator (1200 lines/mm) [14], was used. At ALS, the reflectivity measurements were performed at the *Calibration and Standards Beamline 6.3.2* (bend magnet) dedicated for EUV, soft x-ray reflectometry, and scattering ex-

Figure 4-3: Pole figure measurements of Cr/Sc multilayers grown with three different ion assistance schemes. Each multilayer is comprised of 25 bilayers and has modulation period of 6.4 nm.

periments [19]. Depending on the scanning geometry, four kinds of reflectivity measurements are made in this work and are listed here:

- **angular scans:** are similar to ω-2θ scans in HXR, but are made at near-normal incidence. Here the scans were performed at fixed energies corresponding to the multilayer design parameters.

- **rocking curves:** data was obtained for 1st order Bragg reflections at the fixed energies.

- **energy scans:** were made at fixed θ values. Though the energy scans are illustrious of synchrotrons, reflectivity R(θ) measurements for a fixed wavelength were preferred over a measurement of R(λ) at fixed angle, because $\bar{\eta}$ does not change and thus provides fewer parameters for simulations

- **Bragg scans:** are 2-dimensional scans, made by performing identical $\omega - 2\theta$ scans for different energies over a required energy range. It facilitates to simultaneously scan the Bragg-peak intensity and position with varying energy, and are very useful, especially close to the absorption edges where the reflectivity can change abruptly.

All four kinds of SXR measurements are illustrated in Figs. 4-4 (a)-(d), for Cr/Ti multilayers with $N = 200$ (designed for normal-incidence) in 4-4 (a)-(c) and with $N = 150$ (designed for the Brewster angle $\smile 45°$) in Fig.4-4 (d).

Typically, HXR measurements are preferred over SXR because they allow to probe a larger q range (Eq. 4.1) and are less affected by absorption. However, the roughness features measured by X-ray reflectivity varies non-linearly with operating X-ray wavelengths. In addition, X-ray beams are usually not perfectly monochromatic and collimated, which limits the longitudinal and transverse coherency of X-rays respectively [39]. For grazing incidence measurements the larger longitudinal coherency of X-rays is required to probe the lateral correlations in the multilayer, while at normal incidence the large transverse coherence is beneficial to determine the similar structure. Discrimination of low (jaggedness) and high (waviness)
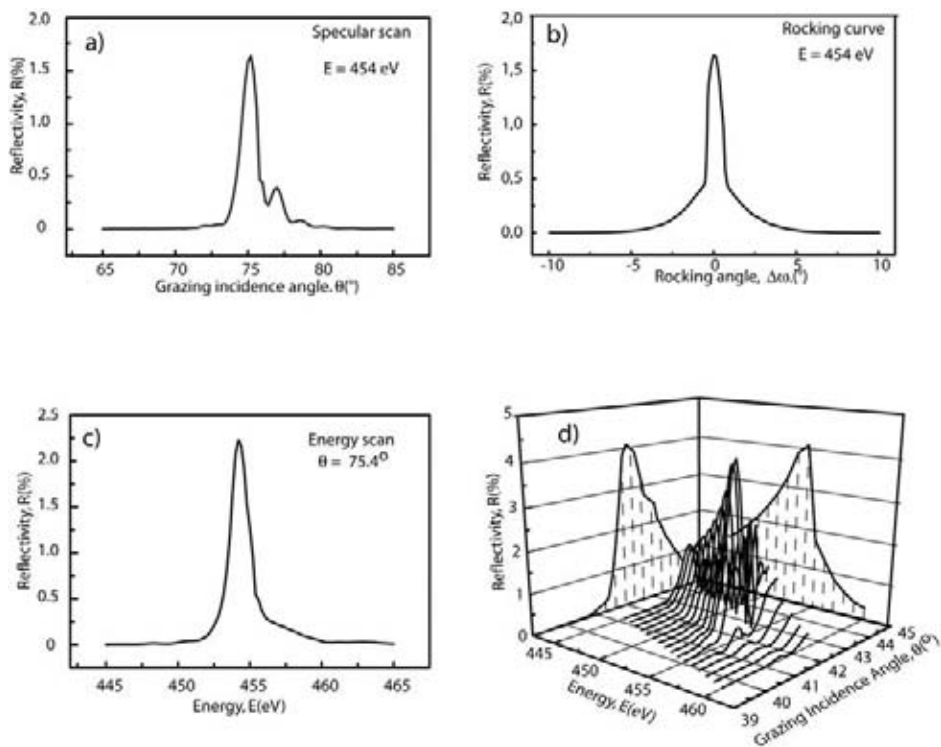
Figure 4-4: Types of measurements made with synchrotron radiation: (a) specular reflectivity scan, (b) diffuse scattering measuement around the specular peak, (c) energy scan, reflectivity peak occurred at the Ti-*2p* absorption edge. The above three measurements were made at near-normal incidence for a Cr/Ti multilayerae with N= 200. (d) A Bragg scan in 3D from which 2D Bragg scan can be derived. Angle and energy profiles are projected on the corresponding axis.

Figure 4-5: Hard X-ray reflectivity measurements ($\omega - 2\theta$) during in-situ annealing up to $600°C$. A Cr/Ti multilayer with 100 bilayers have exhibited highest peak (m=1) reflectivity at room temperature (RT).

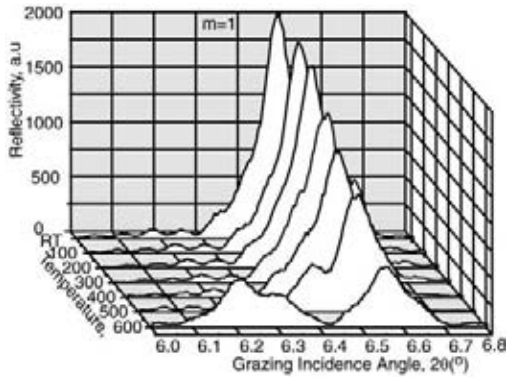spatial frequency roughnesses in Cr/Sc and Cr/Ti multilayers, respectively, was accomplished by comparison of hard and soft X-ray diffuse scattering. Roughness determination on the basis of X-ray wavelengths and X-ray coherence lengths will be further discussed in Chapter 5.

4.1.4 *In-situ* Hard X-ray Reflectivity during Annealing

Thermal stability of the multilayers was investigated using HXR during annealing. Annealing was performed in a Philips X'pert MPD Bragg-Brentano, θ-θ diffractometer with Cu-K$_\alpha$ X-rays equipped with a Bühler HDK 2.4 high temperature, high vacuum chamber with a Be-window. The annealing sequence essentially followed a step wise temperature increase, for regular intervals, from room temperature up to ∼900°C. *In-situ* X-ray reflectivity and diffuse scattering was continuously recorded during annealing and reflectivity curves were further analyzed to extract information regarding structural evolution. An example of reflectivity evolution of the first Bragg peak during annealing is shown in Fig. 4-5 for a Cr/Ti multilayers containing 100 periods. The temperature, in this experiment, was raised in steps of 100°C and the sample was annealed for one hour at each temperature. As illustrated in Fig. 4-5, the first order reflection exhibited a continuous decrement till 400°C, thereafter the multilayer peak was split into two adjacent peaks which moved further apart on increasing the temperature while continuing to decrease in intensity. The Cr/Ti layer system have shown thermal stability only up to ⌣100°C, which is a rather low value for most of the mirror applications. The thermal stability studies of Cr/Sc-based multilayers presented in *Paper V* shows that Cr/Sc-based multilayers may withstand higher temperatures.

4.2 Electron Microscopy

In this thesis cross sectional transmission electron microscopy (XTEM) was extensively used to characterize the structure of individual layers and to image the trend of roughness propagation

when hundreds of interfaces are involved. XTEM images are acquired using either a Philips CM 20 UT microscope equipped with a LaB_6 filament or a FEI Tecnai G2 TF 20 UT field-emission instrument, both operated at 200 kV with a point resolution of 0.19 nm. Cross-sectional samples were prepared by mounting 1x1.8 mm^2 sample pieces in a titanium grid and grinding with a combination of silicon carbide and diamond papers from both sides to a thickness of about 50 μm. Low-angle ion milling, in either a BalTec RES 010 rapid ion etch operated at 8 kV, or a Gatan PIPS operated at 5 kV, was utilized for utilized to make the samples electron transparent. A final polishing stage, using low-energy ions at 2.5 kV, was applied to remove the amorphous surface layers formed in the previous stage. Compositional analysis was carried out using energy dispersive X-ray spectroscopy (EDX), available in the Tecnai instrument. In the following sections I present a brief description of how several TEM operating modes were combined to characterize the samples.

4.2.1   Bright Field and Dark field

Fig. 4-6 (a) and (b) shows example of bright field (BF) and dark field (DF) images from the same area in a sample. These are the two commonly used TEM imaging modes and are obtained by choosing the transmitted (BF) or a scattered (DF) electron beam by placing an aperture in the back focal plane of the objective lens. The principal difference in the imaging modes is the contrast mechanism. When the aperture is placed to include the central transmitted beam, the image formation is due to mass-absorption and diffraction contrasts generated by interference of transmitted electrons. The selection of diffracted (scattered) beam on the other hand form the images consisting of *primarily* diffraction contrast. The images in Fig. 4-6 show a CrN_x/ScN_y multilayer structure comprising of six multilayers of varying layer thickness ratios, Γ, but of a constant modulation period, Λ=1.8 nm. In the BF image a fine layer structure is visible in the multilayers and this is due to the mass contrast where heavier(Cr)/lighter(Sc) elemental layers appear as dark/bright stripes, respectively. Also the multilayer with larger Γ (thicker Cr layer) appear darker and *vice versa* for Sc. The multilayer with Γ_6 appears darker compared to Γ_1, although both have (exactly) the same structural parameters; this is mainly a consequence of the nonuniform sample thickness, where thicker areas appear darker due to "hindered" electron transmission. The microstructure of individual layers in such short period multilayers is not pronounced in BF mode. However, uniform gray areas in DF (e.g. for Γ_4=0.33) shows that either no crystallites are oriented in this area to fulfil diffraction condition or are comprised of very small uniformly distributed crystallites (close to amorphous structure). Contrary to this, the appearance of bright and dark areas in all other Γ values show crystallites formation up on increasing Cr or Sc layer thicknesses.

4.2.2   High Resolution Transmission Electron Microscopy

To obtain lattice resolved high resolution (HRTEM) images at higher magnifications several diffracted and the transmitted beams are required. As opposed to mass/thickness contrast in conventional BF microscopy, image formation in HRTEM, also known as phase contrast imaging, arises from the interference in the image plane of both scattered and unscattered electron beams. The inset in the BF image in Fig. 4-6 (a) shows a lattice-resolved image of the multilayers in multilayer with Γ_5 =0.17. The spots in the HRTEM reveal the ordered arrangement of atoms, indicative of crystal structure in both Cr(dark) and Sc(bright) layers in this multilayer. The phase contrast mechanism has also been used to investigate the abruptness of the interfaces by examining the appearance of Fresnel fringes; the more abrupt interfaces result in fringes of stronger contrast, as is discussed in *Paper 2*.
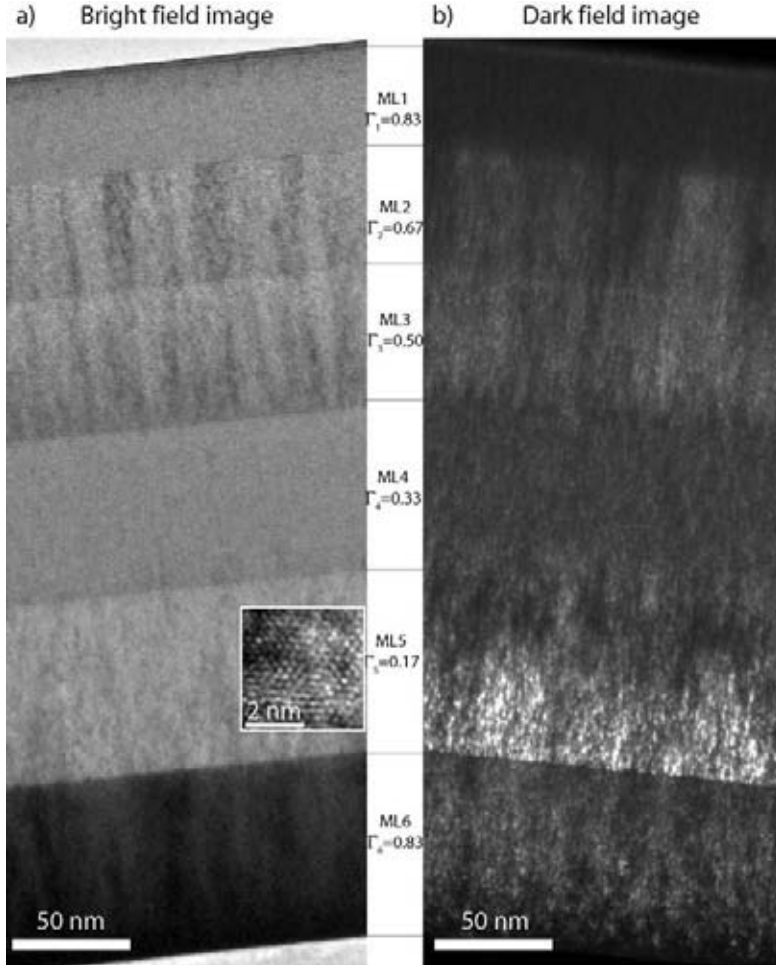
Figure 4-6: The (a) BF and the (b) DF,(from the multilayer reflection in the growth direction) images from the same area in a Cr/Sc stacked multilayer structure constituting six multilayers of different Γ. All the multilayers have same Λ=1.8 nm. The total thickness of the multilayers (Σ) was gradually decreased from multilayer 1 to 6 during the growth. The BF image was formed when all the transmitted and scattered electron beams were selected to be inside of the objective aperture. In the inset a HRTEM image of a multilayer with $\Gamma_2 = 0.17$ is shown.

Figure 4-7: a) The SAED pattern (including the multilayer and the substrate) of stacked mutilayers shown in Fig. 4-6. Bright spots 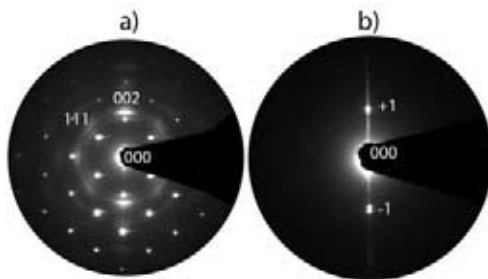are Si reflections. Multilayer diffraction pattern is characteristic of an fcc-structure with strong 002 fiber texture oriented in the growth direction. The SAED is indexed with the 002 and , 111 reflection, (the bright spots are from the Si substrate). b) SAED at long camera length showing the ± 1 orders multilayer reflection, around the central beam.

4.2.3 Selected Area Electron Diffraction

Selected area electron diffraction patterns (SAED) are reciprocal space representations of a selected area from the sample [40]. The ED patterns are formed in the back focal plane of the objective lens from diffracted electrons and are projected to the image plane. The diffraction patterns from areas as small as several hundred nm can be examined by placing small apertures in an area of interest in an image plane below the objective lens. Electron diffraction patterns were routinely used to orient the cross-sectional samples so that the Si substrates [1$\bar{1}$0] zone axis is parallel to the electron beam as in Fig. 4-7 (a). This orientation step was critical to ensure the visibility of sub nm thin multilayers which were grown on top of the Si (001). Moreover, SAED was used to investigate the microstructure (crystalline/amorphous nature) of the multilayers. For example, Fig. 4-7 (a) shows a SAED pattern obtained from the multilayer sample shown in Fig. 4-6. The presence of strong 002 rings indicate an fcc structure and strong fiber texture in growth direction. Additionally, long range structural conformity of multilayer structures can also be investigated by taking SAED pattern at large camera lengths and analyzing multilayer reflections around the central beam as is shown in Fig. 4-7 (b). The intensity spread in the first order reflection spots (n=± 1) in this case is due to a slight variation of modulation period of different multilayer stacks. A more precise determination of layer periodicity was, however, always made by XRR measurements.

4.2.4 Scanning Transmission Electron Microscopy and Energy Dispersive X-ray Spectroscopy

The diffusion in annealed multilayers were studied by scanning (STEM)a focused electron probe (several Å) over areas of interest in TEM. Z (atomic number)-contrast images were obtained by detecting incoherently scattered electrons at high angles with a high-angle annular dark-field (HAADF) detector. The STEM image recorded for a CrN_x/ScN_y multilayers annealed up to $600°$ is shown in Fig. 4-8 [*Paper V*]. The bright/dark regions correspond to high/low average atomic number, respectively. A non-homogeneous contrast in the multilayer as well as at the film-substrate interface indicates that several reactions have occurred upon annealing,
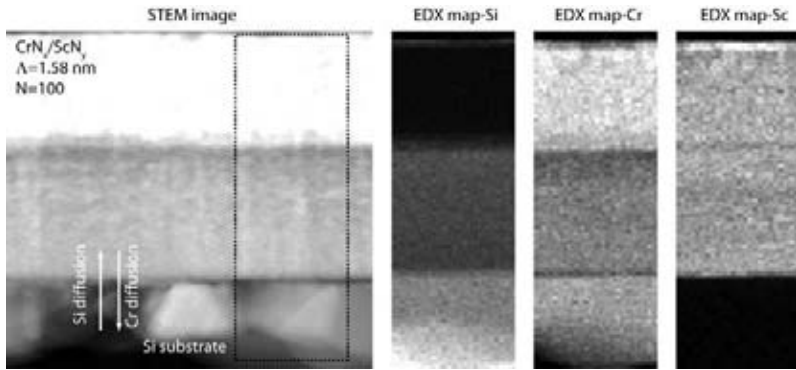
Figure 4-8: The Z-contrast STEM image of an annealed multilayer structure. The Si-Cr diffusion at the multilayer-substrate interface is shown. The rectangular box represent the area where the EDX maps were collected. Accompanying EDX maps show the elemental distributions os Si, Cr, and Sc inside of the multilayer.

for example that Si has diffused into the multilayer.

Further information is revealed by elemental mapping using an energy dispersive X-ray spectrometer (EDX). From the elemental profiles of Si, Cr, and Sc in Fig. 4-8, diffusion of Si up to the middle of the multilayer and Cr into the substrate can be seen in the Si and Cr maps, respectively. The combination of STEM and EDX has thus provided the elemental distribution information after diffusion in thermally treated multilayers, presented in *Paper 6*.

4.3   Ion Beam Analysis

Ion beam (compositional) analysis (IBA) methods are based on the nuclear and electronic interaction between energetic ion beams of several MeV and the targeted material [41]. The resulting emission of particles or radiation and their energies are characteristic of constituent elements and their distribution in a sample. The IBA facilities at *Institute für Ionenstrahlphysik und Materialforschung, FZD, Germany* [42], and *Tandem Laboratory, Uppsala University, Sweden* [43], were used in the present work. Two complementary IBA techniques; elastic recoil detection analysis (ERDA) and Rutherford backscattering (RBS) spectroscopy were used to probe elemental compositions in multilayer structures as a function of depth.

4.3.1   Elastic Recoil Detection Analysis

In ERDA an incident ion beam of tens of MeV is directed, at grazing angles, onto the sample surface. As a result of the bombarding geometry, binary collisions between energetic ions and the target occur and light elements are most likely to be ejected (recoiled) in the forward direction. The atomic number and the energy of the backscattered ions and the recoils can be measured and analyzed to obtain the depth-resolved compositional information. The method is most suitable to detect light elements (including hydrogen) as the heavier elements do not recoil easily and scattered at the latter stage and overlap with the backscattered ions.
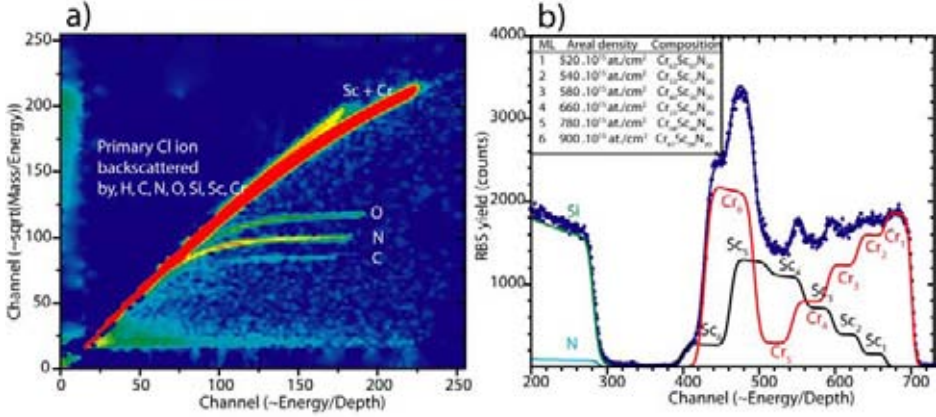
Figure 4-9: Ion beam analysis of a stacked CrN_x/ScN_y multilayer structure (a): A 2D ERDA contour plots, measured by Cl^{+7}ion beam, and (b) RBS spectrum together with simulated elemental concentrations.

ERDA was a primary choice for compositional analysis in this work, mainly due to my interest in tracing light elements incorporated in the multilayers. ERDA was performed either using 35 MeV Cl^{7+} or 40 MeV I^{9+} ion beams at incidence angles of 15° or 22.5° relative to the film surface, respectively. The recoils were analyzed at a scattering angle of 45° relative to the incoming beam direction. The information contained in ERDA spectra is a function of mass, composition and depth, as shown in spectrum in Fig. 4-9 (a) obtained using 35 MeV Cl^{7+} beam from a Cr/Sc multilayer structure. The TEM image of this multilayer structure is shown above in Fig. 4-6. The branches in the spectrum, labelled as C, N, O and Cr+Sc recoils are separable due to their atomic masses and the projection of each branch on the x-axis can be analyzed to obtain the corresponding depth profiles. However, information is limited to $\leq$ 400 nm from the surface due to overlapping scattered Cl ions with the light element signals. Moreover, due to heavy mass of Cl ions used, Cr and Sc are not separable. Large depths can be probed using more energetic Cl ions, whereas heavier ions like I can increase the depth scale of the light elements and resolve individual Cr and Sc.

Though the use of heavier I^{9+} ion beam was advantageous, most of the analysis on stacked multilayers (presented in *Paper IV*) was made using the Rossendorf setup with Cl^{7+}, which gives better detection of lighter elements. For full compositional analysis complementary RBS was performed, particularly for the thick multilayer films.

4.3.2   Rutherford Backscattering Spectroscopy

RBS involves a beam of highly-energetic light ions (2 MeV), typically hydrogen or helium, directed towards the targeted surface at normal incidence angles. The number of elastically backscattered incident ions and their energies provide the information regarding the composition of the sample, distribution of those components, and in some cases the thickness of the sample. Since energetic light ions can be more readily backscattered by heavy atoms, RBS spectroscopy is more sensitive to heavy elements than ERDA and, therefore, was used to determine the

metal content in the multilayers. The RBS measurements were performed using a 1.7-2.0 MeV He$^+$ beam with near normal incidence angle, while the backscattered beam was detected at $\sim$ 170°. For illustration, the number of backscattered He ions as a function of energy is plotted (dotted line) in Fig. 4-9 (b) for the same sample as in (a) together with the best fit (solid blue line) of the measured data and the individual Cr, Sc, Si, and N profiles [44]. Due to lower yield of scattering, individual light elements are not separable and light element composition detected from ERDA analysis is used here for the simulations. As can be seen in the plot, all six multilayer stacks with different Γ can very nicely be separated in RBS, which is not the case for ERDA. The RBS yield and multilayer composition of each stack is also shown in the plot. In this way, a combination of ERDA and RBS analysis was used, e.g. in *Paper IV*, to characterize the composition and density of complex multilayer structures.

Chapter 5

Multilayer Roughness

> *Multilayer materials selection based, only, on optical properties (see Chapter 2) does not guarantee a good quality reflective mirror, mostly because of the inability of the chosen materials to form atomically abrupt and smooth interfaces[1]. This chapter primarily deals with multilayer structural roughness dependence on the chosen materials.*

In principle, heteroepitaxial transition metal (selected on the basis of their optical properties) superlattices presenting geometrically flat and atomically abrupt interfaces would constitute the system of choice for high quality X-ray mirrors [45]. A prerequisite of heteroepitaxy, however, is minimal in-plane lattice mismatch of substrate-film and film-film crystal structures. An example of such a superlattice is CrN/ScN superlattices grown at 735 $^\circ C$ on lattice matched MgO(001) (see *Paper VI*). The HRTEM image and the corresponding diffraction pattern of this superlattice are shown in Fig. 5-1. Lattice mismatch between fcc-CrN and fcc-ScN is $\sim 3\%$ and such a relation does not exist for e.g., pure Cr and Sc crystal structures. In pure transition metal multilayers the lattice mismatch, is usually larger$\sim 10\%$; while typical substrates are either polished quartz or a Si wafer displaying native SiO_2 layer. In such systems epitaxial breakdown occurs at the substrate/metal interface boundaries and non coherent interfaces with large defect densities are formed. Moreover, lower growth temperatures (required for short period multilayer growth) typically result in increased defect concentrations and enhanced surface roughening rates [46].

Appreciating the low temperatures used in this work, high-flux low-energy ion assistance has proven to improve the surface mobility while effectively avoiding bulk diffusion, resulting in denser multilayers with lower defect density and interface imperfections. This is illustrated in the TEM images shown in Fig. 5-2 for the Cr/Ti multilayers (each containing two multilayer stacks with periods of 1.4 and 2.8 nm). The appearance of denser layers and more distinct and sharper interfaces for continuous and modulated ion assistance (described in Chapter 3) can directly be noticed in contrast to the multilayers grown without ion-assistance, and is a plausible explanation for the increase in X-ray reflectivity shown in Fig. 3-7.

The multilayer densification and roughness reduction effects of ion-energy modulation are seen in all short period multilayers presented in this thesis. However, despite of identical optimization of process parameters, certain structural peculiarities are seen for the three material systems used: Cr/Ti, Cr/Sc, and Ni/V. In the next sections, some insight is given into

---

[1]Make sure that the material can be deposited with sharp, smooth boundaries, such that $\sigma < 0.1\ \Lambda$ for the desired multilayer period Λ. *Eberhard Spiller [21]*
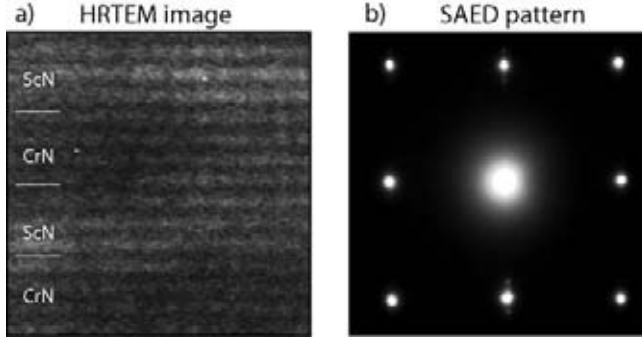
Figure 5-1: (a) HRTEM image grom a CrN/ScN superlattice with the modulation period of Λ of 1.7 nm grown at 735 °C, (b) corresponding selected area electron diffraction pattern obtained along the [010] zone axis.

the correlation and propagation of a few of the characteristic interfacial roughnesses in terms of materials intrinsic properties, kinetic limitations, and intermixing.

5.1 Thermodynamical Roughening

Often, transition metal atoms are characterized by their unfilled d-shells and strong covalent bonding between d-orbitals, unlike alkali metals which have weak bonds made of sp-electrons. As a consequence, transition metals possess comparatively higher cohesive energies and crystal structure occurs in the close-packed fcc, bcc, or hcp arrangements. The cleavage energies or the solid surface free energies, γ, of these elements are also higher and, assuming strain free surfaces at a temperature, T, below the melting point, T_m, γ can be estimated by the empirical rule [47]:

$$\gamma(T) = 1.2\gamma_m + 4.5 \times 10^{-4}(T_m - T), \tag{5.1}$$

where T_m (in J) is the melting temperature and γ_m is the surface energy at the melting point. The melting temperatures and γ_m values of transition metals used in this thesis are listed in Table 5.1, together with other relevant properties. At the interface the surface energies of materials A and B contribute to the interface energy, γ_i, (see Chapter 3) via

$$\gamma_i = E_i + E_D, \tag{5.2}$$

where the energy E_D is associated with eventual defects at the interfaces and E_i is

$$E_i = \gamma_A + \gamma_B - \sqrt{2\gamma_A\gamma_B}. \tag{5.3}$$

Interface energies are always positive and play a crucial role in the arrangement of atoms at the interfaces. It has been reported that a large surface energy difference can result in an enthalpic driving force for intermixing even in systems with a large positive heat of mixing [50]. However, it is difficult to measure the extent of such an interdiffusion to draw any conclusion about interface widths in my short period multilayers. The role of cohesive energy in defining
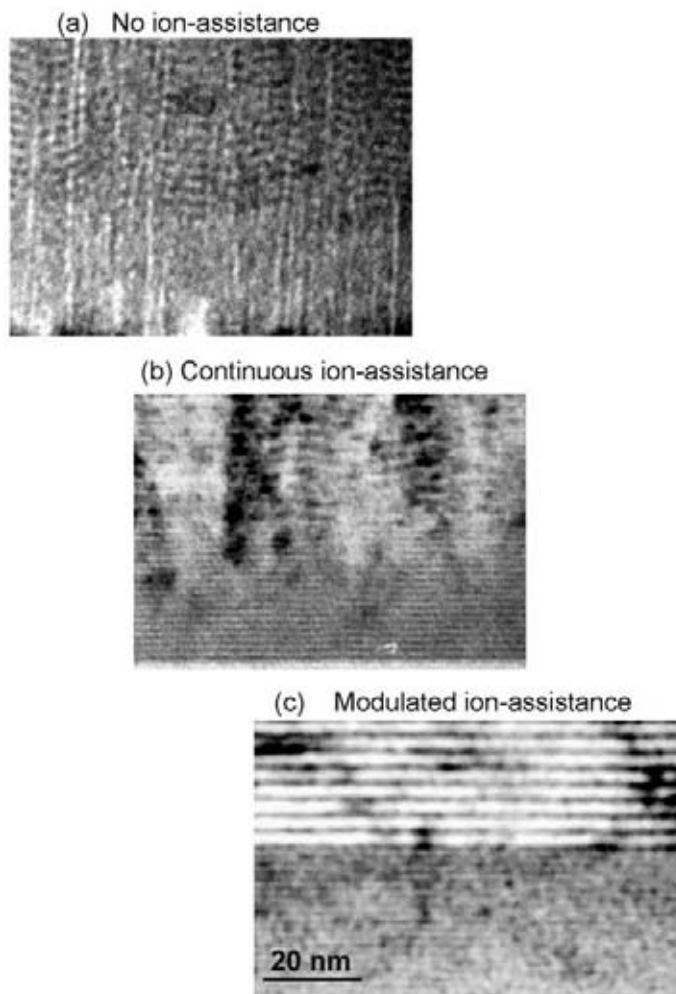
Figure 5-2: TEM images of Cr/Ti multilayer stacks grown with different ion assistances: (a) low ion-to-metal flux ratios < 0.1 and no bias, (b) high-flux ratios > 2, and continuous ion-energy of 22 eV and, (c) high-flux ratios with modulated ion-assistance. Each stack is comprising of two mutilayers: bottom with $\Lambda = 1.4$ nm, and top with $\Lambda = 2.8$ nm.

Table 5.1: Relavent properties of transition metals used in this thesis. The values of surface energies and cohesive energies are taken from [48] and [49], respectively.

Properties - Symbol(units)	Sc	Ti	V	Cr	Ni
Atomic number - Z	21	22	23	24	28
Relative atomic mass- M(g/mole)	44.96	47.90	50.94	52.00	58.70
Crystal structure	hcp	hcp	bcc	bcc	fcc
a, c lattice parameter- (Å)	3.31, 5.26	2.96, 4.74	3.04	2.88	3.524
Melting point - $T_{m}(^{\circ}K)$	1814	1941	2138	2180	1728
RT mass density $\rho(g/cm^3)$	2.99	4.51	6	7.15	8.91
Cohesive enrgy (at 0 K) - (eV/at.)	3.93	4.855	5.3	4.1	4.435
Surface enrgy (at T_m) - $\gamma(J/m^2)$	1.28	2.1	2.55	2.3	2.45

multilayer structure, on the other hand, can indirectly be seen by the degree of crystallization of different materials. Since the depositions in this work were carried out at low temperatures and surface diffusion was governed by low-energy ion bombardment, polycrystalline growth of multilayers with noncoherent interfaces was expected. However, formation of amorphous layers was often observed below certain *threshold* values of the multilayer period and the layer thickness ratios. Threshold thickness varies from one materials system to another, probably depending on the cohesive energies of the constituent materials. For instance, Sc has the lowest cohesive energy of all the materials studied here, and has shown the highest potential to grow amorphous (as long as Λ <2.5 nm and D_{Sc} <1.2 nm), while the rest of the above mentioned metals tend to crystallize at smaller thicknesses.

Another thermodynamical property which governs the probability of intermetallic compound formation at the boundary between two materials is the enthalpy of formation, ΔH. For example Cr-Sc show lower miscibility with ΔH=+1 kJ/mole whereas Cr-Ti exhibit as high miscibility values as ΔH=-11 kJ/mole. The probability of mixing is even higher >-25 kJ/mole for Ni/V multilayers [51].

The roughness associated with intermetallic compound formation and polycrystalline growth with faceted grains at the interfaces is a main concern when assessing small interface widths. Moreover, insufficient adatom mobility at ambient temperatures (T/T_m ∼0.13-0.17) can lead to strongly correlated roughnesses in the growth direction, usually resulting in columnar growth. In Fig. 5-3 some of these observations are illustrated by cross sectional TEM images of stacked multilayers of Cr/Ti, Cr/Sc and Ni/V. The first micrograph in Fig. 5-3 (a), is from a Cr/Ti stacked multilayer showing a dense structures but a low spatial frequency roughness correlation (also known as waviness) all over the sample. In comparison the better interface definition is obvious for each Λ in Fig. 5-3 (b) in Cr/Sc. Our understanding of such roughness evolution stem from the crystallization of the multilayers (most likely driven by the higher cohesive energies of Cr and Ti as well as higher Cr-Ti miscibility), where grains attain a preferred orientation (texture) with increasing multilayer thicknesses and thus give rise to waviness. To some extent, the same reasoning can explain the highly distorted crystalline layered structure seen in the Ni/V multilayer stack. Since, the Ni/V multilayer system has revealed a sensitivity to heating, some layer distortion in the image could be a sample prep artifact.
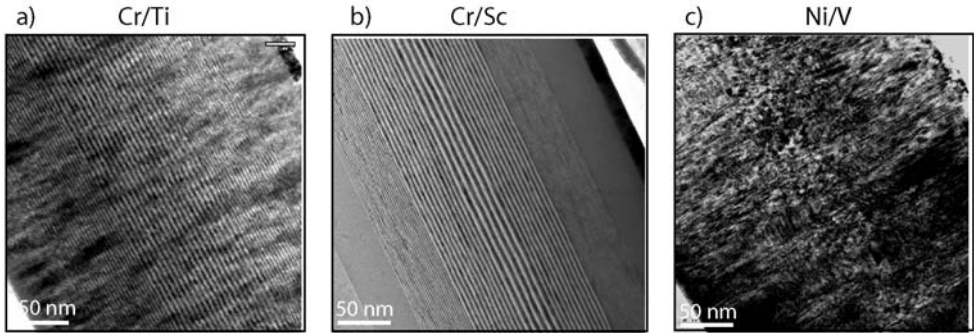
Figure 5-3: TEM overview images of stacked multilayer structures made of Cr/Ti, Cr/Sc and Ni/V. Each stack contains seven multilayers with 4 different Λ values and Γ=0.5. The dark and thick stripe at the upper right corner of Cr/Ti and Cr/Sc stack is a Cr-capping layer. The substrate is at the lower left. Details of the Cr/Sc multilayer structure can be found in *Paper II*.

5.2 Accumulated Roughness

In addition to the modulation period and the layer thickness ratio, the overall roughness of a multilayer has an ultimate dependence on the total number of bilayers [25]. For instance, once established interface roughnesses (classified as jagged or wavy according to the length scale of the lateral roughness correlations, as described in Chapter 2) may accumulate with increasing number of layers in a multilayer, primarily due to diffusion-limited growth kinetics. The distinction between both kinds of prevailing roughnesses is not trivial.

Multilayer roughness scales with X-ray wavelength, almost always; thus,the term *"low /high interface roughness"* refers to the conditions where compositional fluctuations at the interfaces are much smaller/larger than the wavelength of the X-rays. Another important factor is the coherence length of the probing X-rays [1]. Estimations of X-ray coherence lengths for our XRR experimental setups, both parallel, $L_{\parallel}$, and perpendicular, $L_{\perp}$, to the interfaces, show that $L_{\perp}$ is in the order of 0.1 μm for both HXR (λ=0.154 nm) and SXR (λ=2.4-3.1 nm), while $L_{\parallel}$ is in the order of 10 μm for SXR and only 0.025 μm for HXR [39]. Therefore, SXR is more sensitive to low spatial frequency roughness (waviness), whereas atomic scale distortions (jaggedness), have a bigger effect on hard x-ray reflectivities.

An illustration of R(λ) is shown in Fig. 5-4 for the three multilayer systems a)-c) Cr/Ti, Cr/Sc, and Ni/V, respectively. The plots show the evolution of specular reflectivity (for m=1) for both hard and soft X-rays versus the number of multilayer periods in each material system. It can be seen that for the Cr/Ti multilayers SXR saturates at N~50 bilayers, whereas HXR shows the maximum at N=100. The Cr/Sc multilayers in Fig. 5-4 (b), on the other hand, depicts that both X-ray probes follow up to N=300, thereafter HXR exhibits a slight drop. For Ni/V multilayers a sharp increase in HXR for N=100 to 300 followed by a sharp decrease for N≥500 is observed. The SXR of Ni/V multilayers shows an increase, roughly linearly, up to N=500.

It can be concluded that low spatial frequency roughness (waviness) limits soft X-ray reflectivity in Cr/Ti multilayers, while local distortions on the atomic scale, which appear as
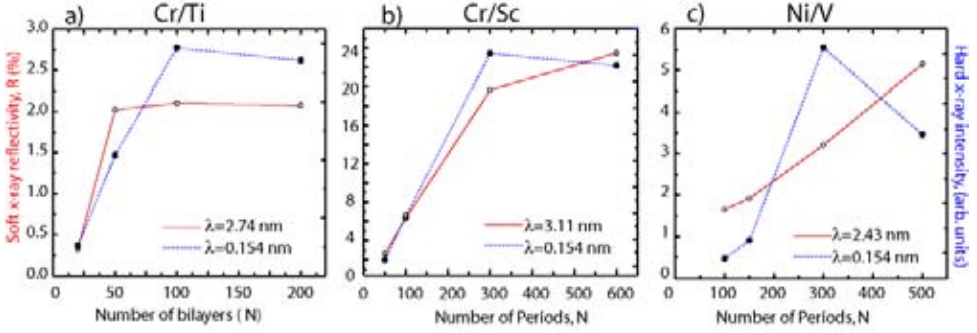
Figure 5-4: Comparison between HXR (dotted) and SXR (solid) reflectivity versus number of bilayers for: (a) Cr/Ti, (b) Cr/Sc, and (c) Ni/V multilayers. At-wavelength SXR reflectivities and HXR intensities are recorded at the first order Bragg peak (m=1).

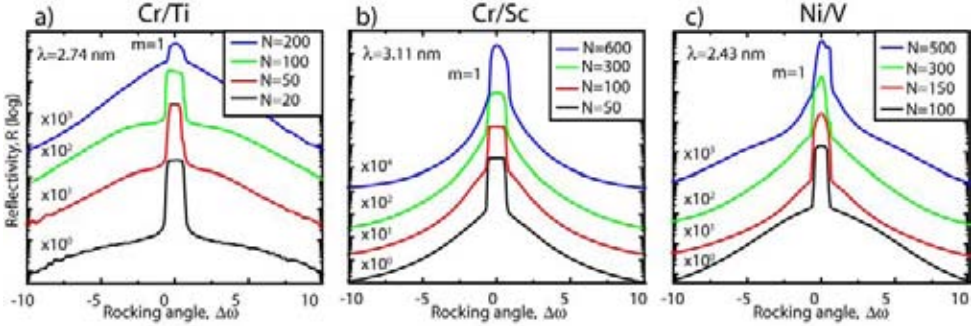intermixed interfaces to soft X-rays, limit HXR in Cr/Sc and Ni/V multilayers.

Figure 5-5: Soft x-ray diffuse scattering comparison of the multilayers shown in Fig. 5-4 for the three material systems. The curves are plotted on log scale and vertically shifted for clarity.

Additional information regarding accumulated roughnesses is gained by qualitative comparison of diffuse scattering measurements. Fig. 5-5 presents the SXR diffuse scans for the corresponding multilayers shown in Fig. 5-4. Recall (see Chapter 2) that the lateral roughness correlation $\xi_\perp$ increases the diffusely scattered intensity around the specular beam, and the correlation length affects the angular distribution of the incoherent halo around the specular direction. These effects are clearly seen in Cr/Ti multilayer where the ratio of specular-to-diffusely scattered X-rays decreases with increasing number of bilayers. This again confirms the accumulation of waviness in this material system with increasing N. For Cr/Sc and Ni/V multilayers, diffuse scattering is much less obvious and there are no major differences in diffusely

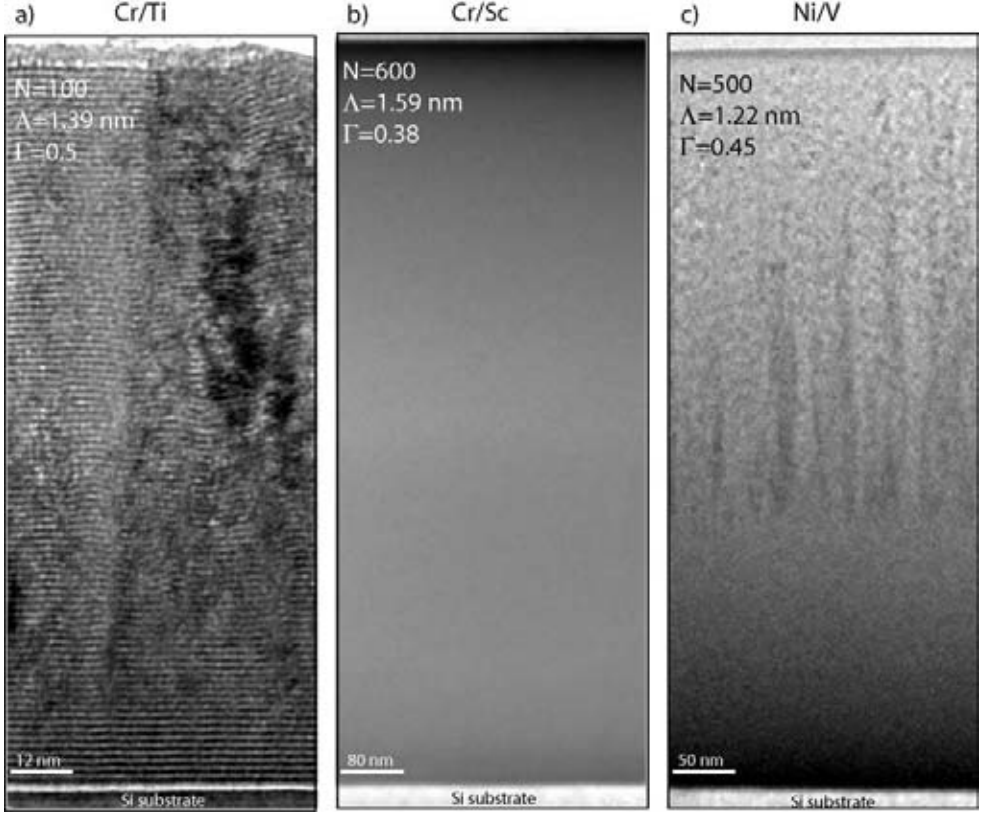scattered x-rays. For Ni/V with N=500, a broadening at the shoulders of the specular peak is observed.

Figure 5-6: Visual illustration of material associated multilayer roughnesses for (a) Cr/Ti, (b) Cr/Sc, and (c) Ni/V. Note the different scales in the TEM images and that each multilayer is composed of different number of bilayers, N.

Fig. 5-6 shows electron microscopy images of Cr/Ti, Cr/Sc, and Ni/V multilayers containing N=100, 600, and 500 bilayers, respectively, providing complementary roughness accumulation information. The TEM image of Cr/Ti multilayer in Fig. 5-6 (a) shows an establishment of a low spatial frequency roughness after N>20, and its accumulation on adding more bilayers while still having locally abrupt interfaces. The image scale roughly depicts $\xi_{\parallel} \backsim 20$ nm while $\xi_{\perp}$ has at some areas, extended throughout the whole multilayer stack which is ~ 140 nm thick. Interestingly, this is not the case for very large N=600 Cr/Sc multilayers as is evident from the absolute homogeneous contrast in Fig. 5-6 (b). No signature of low spacial frequency roughness is apparent in this multilayer. HRTEM images (included in *Paper I*) have, however, shown superior layer definition near the substrate compared to the middle and,
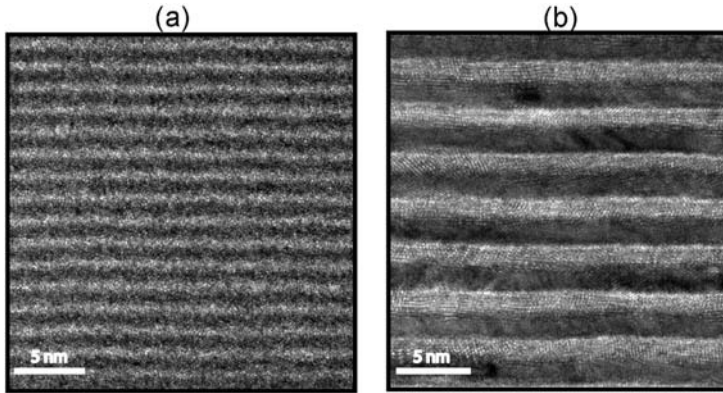
Figure 5-7: Amorphous (a) to crystalline (b) transition of Sc (light) and Cr (dark) layers by increasing bilayer period N from, (a) Λ=1.7 nm to (b) Λ=3.4 nm.

even more, the layers near the top surface. Despite evidence of roughness progression in X-ray reflectivity measurements with increasing N in this system [1], it is not possible to specify any particular kind of irregularity with certainty from the TEM images. The micrograph of Ni/V multilayer depicts two distinct features: an amorphous layer structure for N< 200, and a phase transformation to nano-crystalline layer structure (also shown in *Paper I*) above 200 bilayers. It is evident here that the crystalline nanostructures evolves to columnar growth, but in this case $\xi_{\parallel}$ and $\xi_{\perp}$ are only locally extended, which does not effect diffuse scattering measurements. However, the broadening at the shoulders of the specular peak observed in diffuse scattering scan [Fig. 5-5 (c)] can be attributed to crystallization.

5.3   Intermixing and Interdiffusion

Ion induced intermixing and/or chemically driven interdiffusion govern the degree of compositional abruptness at the interfaces and, hence, the reflectivity via the interface width. Normally, intermixed interfaces lower the specular peak reflectance with a simultaneous decrease in diffuse scattering. HRTEM does not enable analysis of intermixing at the small scales dealt with in this thesis. However, analysis of thicker period multilayers can be used to show the feasibility of intermixed interfaces. This is illustrated in Fig. 5-7 in HRTEM images of Cr/Sc multilayers with Λ=1.7 nm and 3.4 nm. For short periods (which is the main focus of this work) no intermixing can be distinguished, however slightly diffuse Sc-on-Cr interfaces, compared to Cr-on-Sc interface, are evident for Λ=3.4 nm.

Chapter 6

Multilayer Impurities

Light element incorporation and interaction with the constituent layers remains a relatively unexplored area in multilayer mirror fabrication technology. During the final two years of my PhD study, an effort was made to elucidate the influence of residual gas impurities and intentional incorporation of light elements during multilayer growth.

To this point, an assumption of impurity-free multilayers, has been made in describing various aspects of soft x-ray multilayer mirrors, i.e., material choice, mirror design, fabrication technology, growth mechanisms, etc. However, a detectable amount of elements other than the materials of choice is always present in a given multilayer. Contaminated targets, impure sputtering gas, or poor deposition conditions can all contribute to contaminate the multilayers. Although the word "impurity" speaks for unwanted effects of foreign elements for multilayer performance, in certain cases the results are opposite. For instance, it has been reported that incorporation of oxygen during growth of magnetic multilayers [52] enhances the performance of GMR (giant magnetoresistance) devices by altering the growth mode. A small amount of oxygen has, thus, been deliberately added in such multilayers and the term *surfactant* was implemented instead of impurity. For the EUV reflective optics it is found that Mo/Y multilayer mirrors exhibit enhanced reflectivity at λ=9.4 nm when O contaminated yttrium targets were used for magnetron sputter deposition in UHV conditions [53]. The performance of short period soft X-ray multilayer mirrors is expected to be even more sensitive to small structural changes driven by incorporated impurities and, thus, has motivated the research presented in this chapter. In the next section, some of the direct/indirect impacts of light element impurities on multilayer structure and performance are described. The last section, gives a short overview of the experimental setups used in this work to introduce B, C, N, and O, impurities during multilayer growth.

6.1 Light Element Incorporation and Multilayer Mirror Properties

Light element incorporation affects the physical and chemical properties of multilayer X-ray mirrors in several ways. Most of these properties are *inter-dependent*. Fig. 6-1 presents a diagram summarizing the dependency between light element incorporation, interface structure, and optical performance, via fundamental optical and structural properties such as:
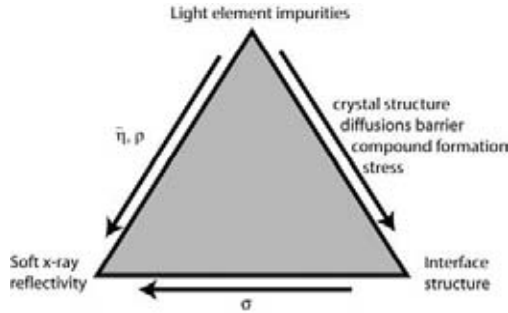
Figure 6-1: Interdependence of light element impurities, interface structure, and optical performance.

Diluted Optical Constants

The most evident effect of impurity incorporation into multilayers is the dilution of the constituent materials with a reduced contrast in refractive index, η, for X-rays, which directly influences mirror reflectance (see Eq. 2.7). This is illustrated in Fig. 6-2 (a) and (b) where dispersion, δ (dotted) and the extinction, β (solid) coefficients of Sc(Cr) are compared with ScN(CrN) i.e., when 50 at.% of nitrogen is incorporated into the metallic elements. The comparison is made in the soft X-ray wavelength range of λ between 1 and 5 nm, which encompasses the absorption edges [1] of Cr (λ=2.18 nm), N (λ=3.08 nm) and Sc (λ=3.11 nm). In Fig. 6-2 (a), an increase in both δ and β for ScN compared to pure Sc can be seen for the entire wavelength region, whereas; CrN in Fig. 6-2 (b) exhibits low δ and β, especially in the region of interest (λ>3.11 nm). A sharp drop in CrN, due to the presence of N, is notable at λ=3.08 nm absorption edge. This drop is not seen in ScN due to the proximity of the Sc and N absorption edges. The combined effect of refractive index, thus, shows reflectivity decrease of $\sim$30% at λ=3.5 nm and $\sim$70% at λ=5.0 nm, from a single Cr/Sc interface (Eq. 2.7) for 50% nitrogen incorporation in these metals. Depending on the material system and on X-ray wavelength, different light elements will have different contributions to the overall refractive index.

Another possible impurity effect is increased X-ray absorption (hence, decreased overall reflectivity) if the impurity absorption edges fall within the λ range of interest. Reflective properties can worsen if the light elements have their absorption edges closer to the wavelengths of interest. For instance, higher extinction just below λ<3.11 nm in CrN is due to a high absorption of X-rays by N, which has absorption edge at λ=3.08 nm. A more general picture of such an impact is shown in Fig. 6-3 where the maximum theoretical reflectivity of Cr/Sc multilayers is plotted for λ=2-8 nm. This materials system exhibits maximum reflectivity of $\simeq$ 64% at λ=3.11 nm (due to anomalous dispersion as a result of $\eta \gtrsim 1$) and for 3.2< λ <8 nm reflectivity of $\sim$25% can be obtained. However, the presence of light element impurities of

---

[1]Sc coefficients are measured experimentally [54] whereas other coefficients are generated [19] assuming bulk densities found in the literature.
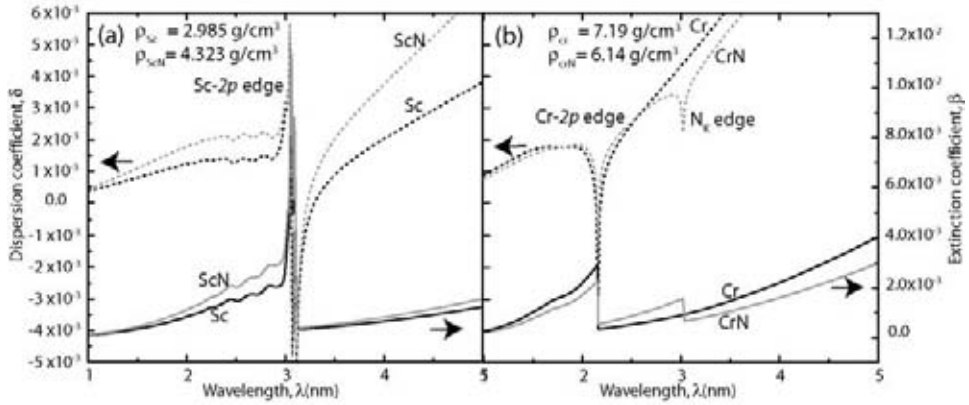
Figure 6-2: Dispersion (δ) (solid) and extinction (β) (dotted) coefficients of: (a) Sc, ScN, and (b) Cr, CrN, plotted near the Sc-2p (λ=3.11 nm) absorption edge in the soft x-ray wavelength range of $1 \leq \lambda \leq 5$ nm.

different natures affects reflectivity in different regions. From the positions of the absorption edge of Cr, O, N, Sc, C and B, indicated (dotted lines) in Fig. 6-3 one can predict that N influences the reflectivity due to its high absorption closer to the Sc edge. Oxygen has high absorption at X-ray wavelengths closer to the Cr absorption edge, whereas C and B effectively absorb X-rays just below their absorption edges.

Structural Transformations

In the process of developing modulated ion-assisted magnetron sputter deposition, the importance of achieving sufficient surface adatom mobility in order to obtain flat and abrupt interfaces has been realized. High-flux bombardment with low-energy sputtering gas ions was used to enhance adatom mobility. However, the nature of the vapor species, i.e., their absorption-desorption characteristics, can also alter the adatom bond strength and therefore contribute in controlling the growth kinetics through called *chemically induced mobility* [55]. A direct impact of modified adatom mobility, in almost all cases, is on the interface morphology (roughness, intermixing) via the alteration in the structural morphology of the multilayers [34].

Chemical interactions of impurities with deposited atoms affect both the growing film thermodynamic (local) equilibrium states and the kinetic paths leading to them. Thus they have the potential to alter the final layer morphology, such as grain size, orientation, crystalline/amorphous transition, and intermetallic compound formation at the interfaces [56]. To some extent, all of these mechanisms affect the interface structure and, hence, the reflectivity of the multilayer via the interface width σ.

Density Variation

Impurity driven structural transformations will affect the density of the multilayers, particularly via amorphous/crystalline transformations. This affects multilayer reflective properties through the refractive index of the constituent materials (Eq. 2.8, and 2.9) which depends
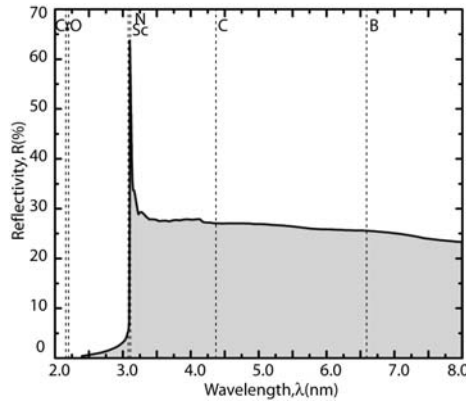
Figure 6-3: Theoretical maximum reflectivities of pure Cr/Sc multilayers in the soft X-ray wavelength region, λ=2-8 nm. The vertical dotted lines indicate the position of the absorption edges of Cr, O, N, Sc, C, and B, from left to right.

linearly on atomic density. The general differences in magnitude of the scattering factors in Fig. 6-2 are indeed a consequence of different crystal structures and, hence, of the density of Cr and Sc upon addition of 50 at.% of N. For example, bulk bcc-Cr has atomic density of $\sim$0.83x10^{23} at/cm^3, whereas fcc-CrN has a Cr density of $\sim$0.56x10^{23} at/cm^3. The reduced atomic density results in lower absorption in CrN [Fig. 6-2(a)] compared to Cr, near the Sc edge. In contrast, fcc-ScN has 20% higher Sc atomic density than pure Sc and this cause a slight increase in extinction coefficient in ScN compared to Sc. However, one has to consider also the dispersion coefficients via the relation Eq. 2.7. in order to (be able to) accurately determine the X-ray reflectivity change with respect to the density (or refractive index) in the multilayer.

Diffusion Barriers

Analogue to surfactants, accumulation of impurities at the interfaces may hinder inter-diffusion of the constituent layers in a multilayer. For example, diffusion in Cr/Sc multilayers, particularly at Sc-on-Cr interfaces (evident in Fig. 5-7), is effectively suppressed by sequentially depositing a thin ($\sim$2Å) B$_4$C layer on top of the Cr layers; resulting in the state-of-the-art Cr/Sc multilayer reflectivity of 31% [57].

Stress Evolution

Stress-driven roughness and adhesion failures are two of the main concerns in multilayer fabrication and can be tuned by light element incorporation. Stress evolution versus light element incorporation has been investigated by David. L. Windt in EUV and soft X-ray mirrors [58], [59]. A profound effect N incorporation on stress in W/ B$_4$C multilayers and residual gas partial pressure dependent stresses in Mo/Si multilayers are, presumably, shown to be a result from the corresponding changes in the chemical composition and microstructure.

Thermal stability

Another effect of light element incorporation, though not related to the reflectance and, hence, not shown in the triangular relation of Fig. 6-1, is on the thermal stability of the multilayers. Several reports have shown that light element incorporation effect the thermal stability of the multilayers via microstructural transformations [60] within the layers or via compound formation (diffusion barriers) at the interfaces [61].

6.2 Related Experiments

A few of the above mentioned effects of light element interaction with the multilayers have been explored during this PhD research. To this end, the influence of continuous incorporation of N, O, C, and B, on the morphology and the optical performance of the multilayers has been investigated. Cr/Sc multilayers were chosen as a model system because of their high potential for practical mirror applications [62], [63] and due to our previous experience with the process parameters, which provides a baseline to compare the impure multilayers. The method for introducing the light elements and the motivation behind each experiment is listed here.

Incorporation of Air: Residual gas impurities are, predominantly, the most natural source and, therefore, needed to be investigated. I have deposited multilayers with different levels of residual gas impurities within the background pressure range of 2×10^{-7} Torr to 2×10^{-5} Torr which was accomplished by tune leaking "clean room air" with controlled H_2O content of 0.87 wt% (corresponding to 60% relative humidity at 20 °C) into the deposition system. The results of this study are presented in *Paper III* and *Paper IV*.

Incorporation of O_2 and N_2: To separate the influence of two major residual gas constituents, i.e., oxygen and nitrogen, depositions were carried out, independently, in pure N_2(99.999%) and O_2(99.995%) background environments. This study is presented in *Paper IV*.

Co-sputtering of B_4C: In contrast to the interleaved B_4C layers as diffusion barriers [57], I have investigated multilayers with 20-40 at% of uniformly distributed B_4C throughout the layered structure. This was achieved by co-sputtering B_4C from a 2 inch magnetron during sequential depositions of Cr and Sc layers. Some of the *unpublished* results from this study are included in Chapter 8.

Chapter 7

Summary and Contribution to the Field

The research work included in this thesis concerns fundamental studies of potential soft X-ray multilayer materials systems. This chapter provides a summary of results and my contribution to the field.

7.1   Cr/Sc-based Multilayers

7.1.1   Effects of Ion Assistance

Paper I and *Paper II* study the structural evolution of Cr/Sc multilayers deposited using different ion assistance schemes. It is shown that the concurrent bombardment of high-flux (Φ_{Cr}=4 and Φ_{Sc}=8) low energy ions (21 eV< E_{ion} <37 eV) during growth can be employed to overcome columnar layer growth and roughening. Significant flattening and distinct interfaces were observed for a range of modulation periods (1.6 nm$\leq \Lambda \leq$10.2 nm), while an amorphous-to-crystalline layer structure transformation above $\Lambda \geq$2.7 nm takes place regardless of eventual ion assistance. It is also shown that Cr/Sc multilayers with periods smaller than $\sim$2 nm are 'self healing', i.e., ion assisted growth results in the recovery of abrupt flat interfaces after morphological disturbances. Near-normal incidence reflectivities as high as R=20.7%, from a multilayer containing N=600 bilayers are achieved. TEM investigations [Fig. 5-6 (b)] and X-ray diffuse scattering analysis [Fig. 5-5 (b)] reveal that short range roughness (jaggedness) accumulation limits the reflectivity for large number of periods in this materials system [64]. For a multilayer designed as a mirror operating at the Brewster angle, a reflectance of R=26.7% and an extinction ratio of Rs/Rp=5450 was obtained.

7.1.2   Cr/Sc Multilayers and Residual Gas Impurities

As discussed in Chapter 6, the presence of light elements in the interior of the layers or at the interfaces alters the structural and optical properties of X-ray multilayer mirrors. The probability of unintentional impurity incorporation in industrial HV deposition systems for mirror fabrication via the sputtering environment is higher; thus, the effects of background pressure on Cr/Sc multilayers were investigated. The multilayers were grown at elevated background pressures ranging from $2.1\mathrm{x}10^{-7}$to $2.1\mathrm{x}10^{-5}$ Torr, by introducing air with a controlled H_2O content of 0.87 wt%.

    Paper III deals with single multilayers with modulation period of 1.6 nm and 100 periods, specially designed as reflective mirrors operating at near-normal incidence at a wavelength

corresponding to Sc-2p absorption edge (λ=3.11 nm). It is shown that pure amorphous Cr/Sc multilayers spontaneously transform into highly textured understoichiometric nano-crystalline CrN_x/ScN_y multilayers at high residual gas pressures of $\sim$2x10^{-5} Torr, due to an incorporation of $\sim$34 at.% of nitrogen. Reduced interdiffusion in the presence of strong nitride bonds leads to abrupt interfaces (SXR) with an average interface width of only 0.29 nm, and a 100 % reflectivity increase in the nano-crystalline multilayers compared to the state-of-the-art amorphous multilayers.

Paper IV describes a multitude of compositional and structural investigations of sophisticated stacked multilayer structures focusing on the effects of modulation period Λ (with constant Γ=0.5), Cr-to-bilayer thickness ratio Γ (with constant Λ=1.8 nm), and residual gas pressure. Based upon comprehensive HRTEM structural investigations and depth-resolved compositional analysis by ERDA and RBS, it is shown that there are no remarkable deferences in structure and composition of multilayers deposited at chamber pressures ranging from 2x10^{-7} to 2x10^{-6}Torr. The amorphous-to-crystalline layer structural transformation above $\Lambda \approx$2.7 nm (also reported in *Paper II*) is found to be independent of pressure changes within this range. From analyses of multilayers with respect to Γ, it is seen that crystallization of Cr/Sc multilayers above a threshold period value is predominantly governed by Cr, most likely due to its higher cohesive energy than Sc.

Depth-resolved compositional analysis has shown that nitrogen is always the most abundant impurity element found in the multilayers, irrespective of deposition conditions, and that it is located predominantly in the interior of the Sc layers due to its higher affinity to Sc than Cr. N incorporation of $\sim$30-35 at% similar to the multilayers presented in *Paper III* at higher background pressures ($\sim$2x10^{-5} Torr) is shown to cause nano-crystallization in multilayers with 0.9$\leq \Lambda \leq$4.5 nm, and 0.17$\leq \Gamma \leq$0.83. A TEM micrograph of such stacked multilayers is shown in Fig. 7-1. The crystalline nature of multilayers is clear from the TEM images and from the corresponding SAED patterns [six multilayers of varying periodicities (a), and layer thickness ratios (b)]. Crystallization occurs through the formation of a CrN_x/ScN_y layered structure with varying degree of texture depending on Λ, Γ, and N content.

The higher reflectivity of the multilayers grown with impurities incorporated from air (in *Paper III*) prompted the need for further investigations on the separate influence of major residual gasses i.e., N_2 and O_2. It is found that, like in the case of air, the multilayers grown with pure N_2 background levels exhibit higher reflectivities whereas oxygen does not significantly interact with the multilayers and has very little influence on reflective properties. These results are included in *Paper IV*.

7.1.3 *Ab initio* Calculations

Understanding the phenomenon of amorphous metallic layer formation, below the transition threshold period $\sim$ 2.7 nm has been of fundamental concern in this research. After showing that amorphization is independent of both ion assistance (*Paper II*) and interaction of residual gas species in a HV deposition environment (*Paper III*), the need to perform theoretical calculations was realized. In collaboration with the group of Prof. Igor Abrikossov at IFM, the *ab-initio* calculations on a number of layers of Cr and Sc lattices coherently arranged with a body centered tetragonal (bct) symmetry of bcc-Cr and fcc-Sc rotated at 45° in (001) were performed. This layered arrangement of Cr/Sc was previously suggested by T. Gorelik *et. al.* through TEM investigations [65]. However, according to our results, formation of coherent interfaces in Cr/Sc multilayer system is unlikely to be realized for any bilayer thickness. Moreover, by calculating interfacial energies we suggested that short period multilayers indeed may eliminate high energy coherent interfaces between crystalline Cr and Sc by creating disordered interfaces i.e., by amorphizing the metal layers. The initial results of the calculations are included in *Paper IV*.
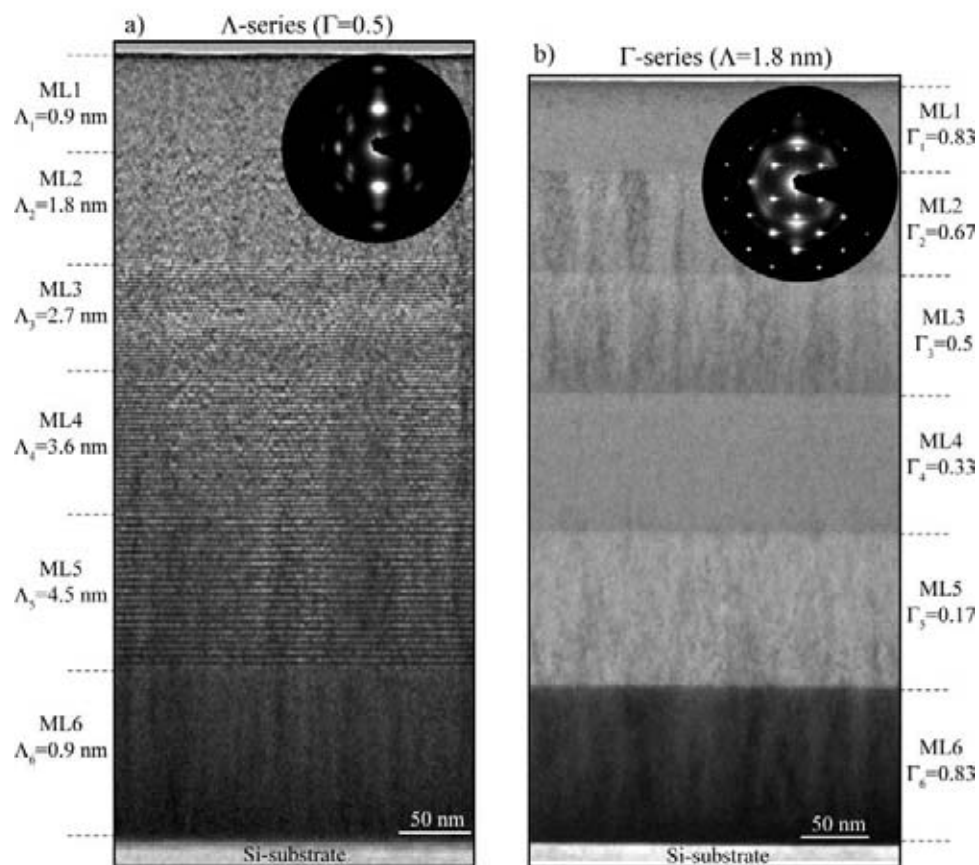
Figure 7-1: Bright field TEM images of stacked Cr/Sc multilayers with: (a) varying periodicities (constant Γ=0.5), and (b) varying layer thickness ratios (constant Λ=0.5). Multilayers were grown at a background pressure of 5×10^{-5} Torr and contains >30at.% of N. The bright (Sc) and dark (Cr) stripes in the images are stem from mass absorption contrast. SAED patterns are shown at the top right of each image.

7.1.4 CrN/ScN Superlattices

Paper VI presents a study of single crystal CrN/ScN superlattice films with modulation periods of 1.64 nm, grown by reactive sputtering in N atmosphere onto MgO(001) substrates. A process window for synthesis was found at 735 °C. Extreme fluxes (Φ_{CrN} =42 and Φ_{ScN}=144) of very low energy (E_{ion}(CrN)=24 eV, E_{ion}(ScN)=28 eV) nitrogen ions towards the growing film surface were found to be beneficial for highly ordered superlattice growth, resulting in minimal interface widths of 0.2 nm. As-deposited superlattices with only 61 periods exhibit an absolute soft X-ray reflectance of 6.95% at λ=3.11 nm (Sc-*2p* absorption edge). These superlattices have shown very high thermal stabilities up to 850 °C as well as higher hardness values of ~19 GPa (as compared to ~5 GPa for pure Cr/Sc).

7.1.5 Thermal stability

The ability to withstand high-power X-rays without suffering damage, such as undergoing interdiffusion of layer components, is important for X-ray mirrors and is investigated in *Paper V* for pure Cr/Sc and CrN$_x$/ScN$_y$ (N=34 at.%) multilayers. Structural changes at elevated temperatures were investigated by *in-situ* HXR (recorded for ~12 hours at each temperature from RT to ~600 °C, with intervals of 50 °C) and *ex-situ* TEM characterization of annealed multilayers.

It is shown that Cr/Sc multilayers exhibit a gradual drop in reflectivity starting at temperatures as low as 100 °C, which vanishes completely at 500 °C. The intensity evolution of the first Bragg peak during sequential annealing of a Cr/Sc multilayer is plotted in Fig. 7-2 a). Though there have been reports on Cr/Sc multilayers showing reasonably high stability up to 280 °C, correlated to the low miscibility of Cr and Sc, our reflectivity measurements and TEM characterization of annealed multilayers reveal that the phase separated nano-crystallite grain formation at the expense of complete elimination of the layered structure is indeed the real cause of the observed reflectivity reduction in pure Cr/Sc multilayers [66].
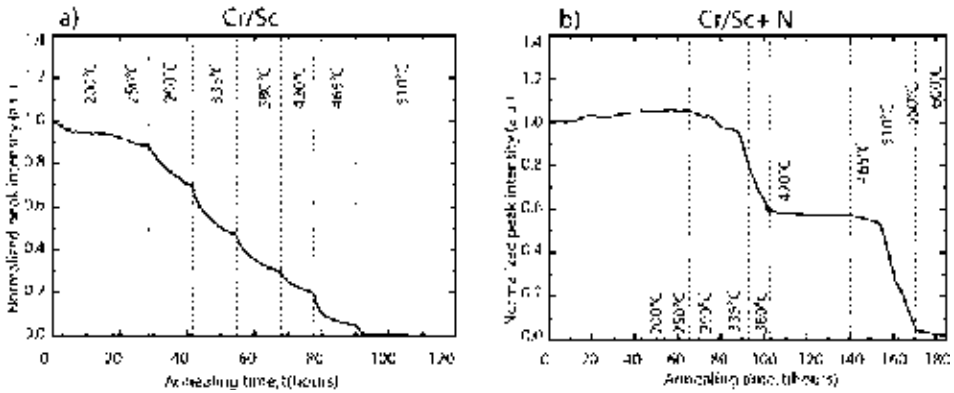

Figure 7-2: *In situ* reflectivity evolution of the intensity of the first order Bragg peak intensity during sequential annealing of a) pure Cr/Sc, and b) Cr/Sc+N(34 at.%) multilayers containing 100 bilayers. Annealing temperatures are given in the graphs. The peak reflectance is normalized to the as-deposited value.

Nitrogen incorporation has shown remarkable improvement in terms of thermal stability of Cr/Sc multilayers. As can be seen in the Fig. 7-2 (b), CrN_x/ScN_y multilayers are stable up to 335 °C after 40 hours annealing. TEM analysis show that the layered structure in this multilayer persists after more than 100 hours of annealing at 550 °C.

In both cases, the reflectivity losses at ∼500 °C were accompanied by a substrate-multilayer reaction. The extent of Si-in and Cr(Sc)-out diffusion, investigated by EDX elemental mapping is found to be highly dependent on multilayer microstructure and composition.

7.2 Cr/Ti Multilayers

Investigations of titanium-based multilayer mirrors were initiated due to the expected establishment of a Ti-based Čerenkov X-ray source [67]. In this regard Cr/Ti multilayer growth was optimized for ion energies and ion fluxes to fabricate normal-incidence mirrors and polarizers (see Fig. 5-2).

Paper *VII* presents the study on Cr/Ti multilayers. Roughness effects associated with the increasing number of bilayers in this materials system were investigated and it is concluded that the number of periods in a Cr/Ti multilayer that can be grown without dominant effects of evolving roughness is limited to ∼100 bilayers. Low spatial frequency roughness is found to be accumulating with increasing number of periods, limiting the reflectivity to 2.1% at λ=2.74 nm (Ti-*2p* absorption edge), which was the highest reported near-normal reflectivity for this short wavelengths at the time of publication. Thermal stability studies show (Fig. 4-5) a decrease in reflectance of Cr/Ti multilayers already at T >100 °C.

7.3 Ni/V Multilayers

Ni/V multilayers were mainly studied as X-ray multilayer optics operating at even shorter X-ray wavelengths (λ= 2.4 nm, V-*2p* absorption edge). *Paper I* and *Paper VIII (not included here)* address the growth optimization of Ni/V multilayer system. It is shown that this short period multilayers exhibit soft X-ray near-normal incidence (with Λ=1.2 nm) reflectance of R=2.7% at the V-*2p* absorption edge, which is the highest reported value, to date, for such short wavelengths. Multilayers optimized for the Brewster angle (with Λ=1.7 nm) showed a reflectance of R=10% and Rs/Rp=4190. TEM structural studies of this materials system has not been very conclusive due to multilayer adhesion failures and artifacts of slight heating during TEM sample preparation. However, it is concluded [Fig. 5-6 (c) and Fig. 5-5 (c)] that for Ni/V the initial growth is amorphous and the layers turn crystalline after > 200 bilayers with an accumulating low spatial frequency roughness, which limits the reflectivity.

Chapter 8

Additional Results and Future Outlook

In addition to what is presented in the articles in this thesis I will also take the opportunity to present a few, *yet unpublished*, results which can be of interest in conjunction with this thesis.

8.1 Cr/Sc Multilayer Condenser Mirrors

The very first experiments of my PhD studies were focused on attaining high lateral uniformity of deposition fluxes over the 65x65 mm^2 area in an unbalanced dual-cathode magnetron sputter system with small sputtering targets (3"). The lateral thickness uniformity was optimized by iterating the deposition fluxes (by adjustable masks, placed in front of each magnetron) and magnetic configuration (by magnetron-substrate solenoid coupling). HXR profiles over the substrate area were compared for peak positions and intensity to map thickness uniformity. Moreover, a technique to characterize spherically shaped substrates by HXR [68] analysis was developed.

With this knowledge, a *usable* normal-incidence multilayer condenser mirror was fabricated for soft X-ray microscopy applications based on N and C line-emission sources [5], in collaboration with the *Department of Biomedical and X-ray Physics at the Royal Institute of Technology (KTH), Stockholm.* A spherically polished glass substrate with a diameter of 65 mm and a radius of curvature of 241 mm was deposited with Cr/Sc multilayers. Fig. 8-1 shows measurements of at-wavelength absolute near-normal reflectivity versus mirror radius made at Advanced Light Source (ALS). A thickness variation as low as 0.6% over the whole sampled area was achieved, and an average reflectivity of 0.5% was measured at near-normal incidence, while a peak reflectivity of 0.6% was obtained 15 mm from the center. The two main factors limiting the reflectivity are the higher surface roughness ($\sigma \backsim 0.48$ nm) of glass substrates as compared to Si substrates ($\sigma \backsim 0.1$ nm) and the insulating nature of glass substrates, which made it difficult to control the ion-bombardment on growing layers. However, in the future, these obstacles can be overcome by using spherically polished Si substrates.

8.2 B$_4$C Co-sputtering of Cr/Sc Multilayers

Deposition of thin B$_4$C interleaved layers on top of Cr layers has been shown to enhance the SXR and is believed to be due to reduced Cr diffusion into Sc layers, resulting in small interface widths $\sigma \sim 0.24$ nm in Cr/Sc multilayers [57]. In order to investigate the actual mechanism governing
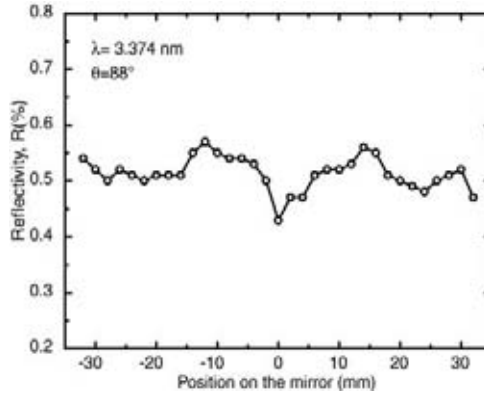
Figure 8-1: Reflectivity variation over a 65 mm. diameter mirror (λ=3.374 nm, θ =88°).

interface quality enhancement, I have studied B_4C incorporation in Cr/Sc multilayers. Instead of depositing thin (2 Å) layers on the top of each Cr layer, B_4C was continuously distributed in both Cr and Sc layers by co-sputtering (see Chapter 6). The amount of B_4C in the multilayers was varied by changing the magnetron power and the exact compositions in the deposited multilayers were determined by ERDA. Fig. 8-2 (a) shows HXR and SXR peak reflectivity of multilayers, comprised of 100 bilayers, versus elemental concentration of B_4C. Approximately 70% increase in both reflectivity values were obtained from multilayers containing 20-40 at.% of B_4C compared to pure Cr/Sc multilayers. In contrast to nitrogen incorporation [Fig. 7-1 (a)], TEM observations of a stacked multilayer with 23 at.% of B_4C in Fig. 8-3 show an amorphous layered structure for all periods in the range of 0.9$\leq \Lambda \leq$4.5 nm. This elemental composition of B_4C is in agreement with the expected quantity of *metalloid* often required to amorphize metal layers [69]. The amorphous nature is evident both, from the homogeneous contrast in the BF TEM image and from the characteristic diffuse rings (double rings could be due to two different length scale of short range ordering) in the diffraction pattern around the central beam (inset in Fig. 8-3). An interruption in B_4C supply during growth resulted in pure Cr/Sc layers of metals displaying its inherent nano-crystalline layer structure, as shown in the marked areas in Fig. 8-3 at the top of the 3rd ML with Λ_3=2.7 nm and in the middle of the multilayer with Λ_4=3.6 nm. These observations clearly show that B_4C incorporation effectively: (a) hinders Cr diffusion into the, resulting into more abrupt interfaces, and (b) prevents crystallization of both Cr and Sc, giving smoother interfaces. The combined effect is a reduced σ and thus increased reflectivity. Our understanding is that these effects are a consequence of the formation of molecular non-metallic species with low mobility and highly directional bonds, which promotes amorphization.

Furthermore, annealing experiments have shown [Fig. 8-2 (b)] that Cr/Sc+B_4C multilayers exhibit 40 % improved reflectivity upon increasing temperature up to 290°C, as well as thermal stability as high as understoichiometric nano-crystalline CrN_x/ScN_y multilayers (up to 350 °C). These results were recently presented in an international conference (*PXRMS 2008 [70])* and are included in *Paper IX (manuscript in preparation)*.
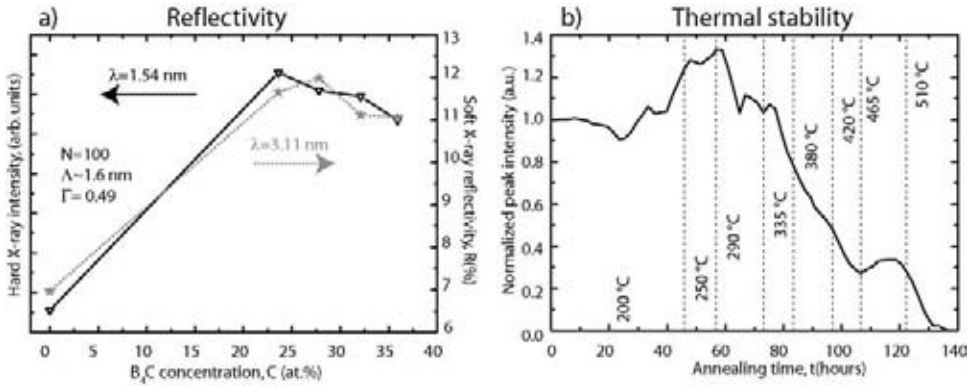
Figure 8-2: (a) First order (m=1) hard x-ray (left y-axis) and soft x-ray (right y-axis) Bragg peak reflectivities of multilayers containing 100 bilayers versus B_4C content. (b) *In situ* reflectivity evolution of first order Bragg peak intensity during sequential annealing of Cr/Sc +B_4C (23 at.%), multilayers.

8.3 Mo/Si EUV Multilayers

Mo/Si multilayers were investigated with the aim to extend the two-stage modulated ion assistance process to the comparatively thicker layers required for EUV mirrors[1]. Multilayer design and deposition parameters were optimized for maximum reflectance at $\lambda = 12.5$ nm. At-wavelength synchrotron radiation measurements were made at BESSY and a maximum reflectance of a 60% was achieved for a multilayer with $N = 50$ bilayers [71], as shown in Fig. 8-4 (a). Even though this value is not as high as the current record ($\sim$70%) a fundamental investigation of ion-energy effects on layer formation of alternating high, (Mo) and low (Si) Z materials was carried out.

    For example Mo/Si multilayers *(unpublished results-Paper X)* grown by modulated ion assistance consist of amorphous Si and polycrystalline Mo, as shown in the TEM micrograph of Fig. 8-4 (b). A rough Mo-Si interface, while excluding intermixing or silicide formation, is attributed to polycrystalline Mo [72]. The key for getting smooth surfaces in this case is the densification of the Mo layers, for instance, by energetic ion-bombardment, into larger crystallites. It is worth mentioning here that the Mo crystallization into larger grains would also have a positive effect on the reduction of silicide formation, i.e., there will be less interdiffusion of the two materials and more abrupt interfaces could be achieved.

8.4 Low Temperature Growth

Paper II and *Paper IV* show that amorphization of short period Cr/Sc multilayers does not depend on ion-assisted growth or incorporation of residual gas species at ambient temperatures, and is suggested to be a result of free energy minimization in the presence of high interface-density. The growth temperature impact on microstructural transition in Cr/Sc multilayers

---

[1]This work was carried out in collaboration with Jordi Romero Mora during his internship project [71].
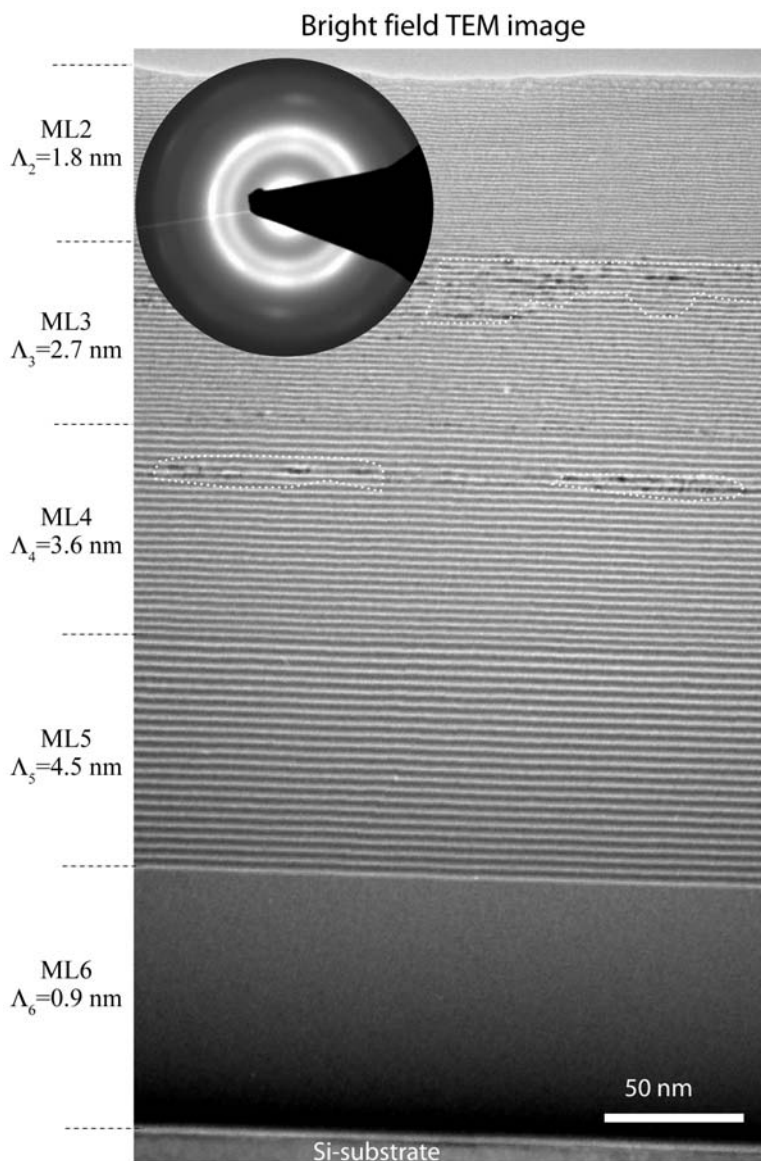
Figure 8-3: Bright field TEM image of a stacked multilayer structure of Cr/Sc multilayers containing 23 at.% of B_4C. Multilayers have constant $\Gamma=0.5$, but different periods l $\Lambda_1=0.9$ (not shown), $\Lambda_2=1.8$, $\Lambda_3=2.7$, $\Lambda_4=3.6$, $\Lambda_5=4.5$, and $\Lambda_6=0.9$ nm. Crystalline pockets due to B_4C flux interruption during growth are marked by dotted lines. SAED pattern is shown at the top left of the image.
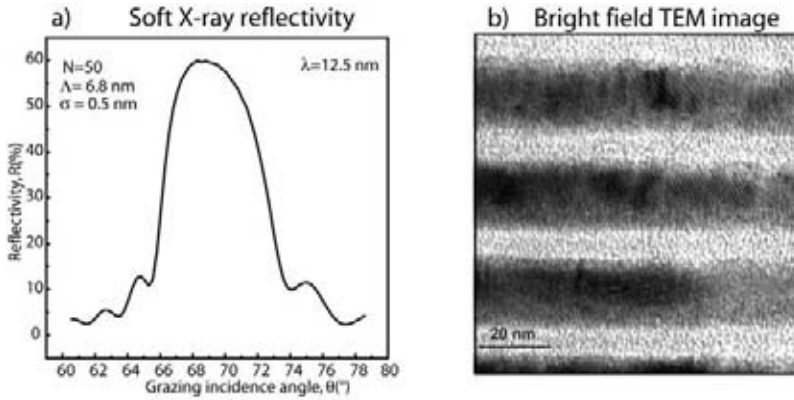
Figure 8-4: (a) Reflectivity profile of a Mo/Si multilayer, measured at $\lambda = 12.5$ nm. The average interface width, $\sigma = 0.5$ nm, is determined by IMD simulations (not shown here). (b) TEM image of Mo (dark) and Si (light) multilayers with modulated period $\Lambda = 6.9$ nm. Dark regions inside the Mo layers are due to the presence of crystallites (diffraction contrast). Light gray areas dominant at Si-Mo interfaces indicate silicide formation.

was also considered in this work. It was suggested that lowering the "bulk" mobility, i.e., inside the layers,(with maintained adatom mobility through low energy ion-assistance) by lowering temperature may extend the threshold period thickness for amorphization. For this purpose, depositions on LN_2 cooled Si substrates were made in UHV conditions[2]. Although a higher accumulated roughness due to reduced mobilities was expected, HXR and TEM analysis showed comparatively smoother interfaces than for the multilayers grown at room temperature. Furthermore, it was found that the reduced impurity level at UHV conditions and/or reduced sub-surface mobilities does not extend the threshold thickness for amorphous multilayers. The results of this study are still in analyzing stage and require more dedicated experiments, e.g., multilayer growth with different ion assistance schemes (*Paper II*) at low temperature will help to understand the smoothening mechanisms.

---

[2]Depositions were made at the Department of Physics at Uppsala University.

Bibliography

[1] F. Eriksson, Soft X-ray multilayer mirrors, Ph.D. thesis, Linköping Studies in Science and Technology, Dissertation No. 875, ISBN: 91-7373-950-2, ISSN: 0345-7524, Sweden (2004)

[2] G. A. Johansson, A. Holmberg, H. M. Hertz, M. Berglund, "Design and performance of a laser-plasma-based compact soft X-ray microscope," Rev. Sci. Instr., **73**, 1193 (2002)

[3] W. Knulst, O. J. Van der Weil, J. Verhoeven, "A tabletop soft X-ray source based on 5-10 MeV LINACS," Proceedings EPAC (2000)

[4] K. Nakajima, "Compact X-ray sources: Towards a table-top free-electron laser," Nature Phys., **4**, 92 (2008)

[5] M. Berglund, L. Rymell, M. Peuker, T. Wilhein, H. M. Hertz, "Compact water-window transmission X-ray microscopy," J. of Mic., **197**, 268 (2000)

[6] E. Spiller, D. G. Stearns, M. Krumrey, "Multilayer X-ray mirrors: interfacial quality," Appl. Phys., **74**, 107 (1993)

[7] J. Chun-Shui, W. Zhang-Shan, C. Jian-Lin, "Soft X-ray projection lithography technology," High power laser and particle beams, **12**, 559 (2000)

[8] http://www.lmsal.com/SXT/homepage.html, Accessed 15 March. (2008)

[9] M. D. Resen, P. L. Hagelstein, D. L. Matthews, E. M. Campbell, A. U. Hazi, B. L. Whitten, B. MacGowan, R. E. Turner, R. W. Lee, "Exploding-Foil Technique for Achieving a Soft X-ray laser," Phys. Rev. Lett., **54**, 106 (1985)

[10] H. E. Bennet, J. M. Bennet, Physics of This Films, Academic, edited by G. Hass and R. E. Thun, Academic, New York, **4**, (1967)

[11] D. Attwood, Soft X-rays and Extreme Ultravoilet Radiation, Cambridge University Press ISBN 0-521-65214-6 (1999)

[12] H. M. Hertz, L. Rymell, M. Berglund, G. A. Johansson, T. Wilhein, Y. Platonov, D. Broadway, "Normal-incidence condenser mirror arrangement for compact water-window x-ray microscopy," Proc. SPIE, **3766**, 247 (1999)

[13] H. M. Hertz, M. Berglund, G. A. Johansson, M. Peuker, T. Wilhein, H. Brismar, "Compact water-window X-ray microscopy with a droplet laser-plasma source," AIP Conference Proceedings 721 (2000)

[14] F. Schäfers, H.-Ch. Mertins, A. Gaupp, W. Gudat, M. Mertin, I. Packe, F. Schmolla, S. Di Fonzo, G. Soullié, W. Jark, R. Walker, X. Le Cann, R. Nyholm, and M. Eriksson, "Soft X-ray polarimeter with multilayer optics: complete analysis of the polarization state of light," Appl. Opt. **38**, 4074 (1999)

[15] B. D. Cullity, Elements of X-ray Diffraction, 2nd edition, Addison-Wesley (1978)

[16] J. H. Underwood, T. W. Barbee, "Layered synthetic microstructures as Bragg diffractions from X-rays and Extreme ultraviolet: theory and predicted performance", Appl. Opt., **20,** 3027 (1981)

[17] M. Yamamoto, T. Namioka, "Layer-by-layer design method for soft-X-ray multilayers", App. Opt., **31,** 1622 (1992)

[18] H. J. Stock, G. Haindl, F. Hamelmann, D. Menke, O. Wehmeyer, U. Kleineberg, U. Heinzmann, P. Bulicke, D. Fuchs, G. Ulm,"Carbon/titanium multilayers for soft X-ray mirrors for the water window," Appl. Opt., **37**, 6002 (1998)

[19] http://www.cxro.lbl.gov, Accessed 15 March (2008)

[20] D. L. Windt, "Computers in Physics," **12**, 360 (1998)

[21] E. Spiller, Multilayer optics for X-rays, Physics, fabrication and Applications of Multilayered Structures, (1988)

[22] D. G. Stearns, D. P. Gaines, D. W. Sweeney, "Nonspecular X-ray scattering in a multilayer-coated imaging system", J. Appl. Phys. **84**, 1003 (1998)

[23] D. G. Stearns, "The scattering of X-rays from nonideal multilayer structures," J. App. Phy. **65**, 491 (1989)

[24] V. Holý, T. Baumbach, "Nonspecular X-ray reflection from rough multilayers," Phy. Rev. B, **49**, 10669 (1994)

[25] A. Paul, G. S. Lodha, "Interface roughness correlation due to changing layer period in Pt/C multilayers", Phy. Rev. B, **65,** 245416 (2002)

[26] S. K. Sinha, E. B. Sirota, S. Garoff, "X-ray and neutron scattering from rough surfaces," Phy. Rev. B, **38**, 2297 (1998)

[27] J. E. Greene, Hand book of crystal growth, edited by D. T. J. Hurle, North-Holland, Amsterdam, Vol. **1**, (1993)

[28] J. E. Greene, S. A. Barnett, J.-E. Sundgren, A. Rockett, Ion-beam assisted film growth, edited by T. Itoh, Elsevier, Amsterdam,Vol. **1**, (1988)

[29] C. Engström, Nitride Based Superlattices, Ph.D. thesis, Linköping Studies in Science and Technology, Dissertation No. 537, ISBN/ISSSN 9172192259, Sweden (1988)

[30] C. Engström, T. Berlind, J. Birch, L. Hultman, I. P. Ivanov, S. R. Kirkpatrick, S. Rohde, "Design, plasma studies, and ion assisted thin film growth in an unbalanced dual target magnetron sputtering system with a solenoid coil," Vacuum, **56**, 107(2000)

[31] E. B. Svedberg, J. Birch, C. N. L. Edvardsson, J. E. Sundgren, Surf. Sci., **431** (1999)

[32] B. Chapman, Glow Discharge Processes, Wiley, New York (1980)

[33] X. W. Zhou and H. N. G. Wadley, "Atomistic simulations of low energy ion assisted vapor deposition of metal multilayers," J. Appl. Phys. **87**, 2273 (2000)

[34] N. Kaiser, "Review of the fundamentals of thin-film growth," Appl. Opt. **41**, 3053 (2002)

[35] W. Ensinger, "Low energy ion assist during deposition- an effective tool for controlling thin film microstructure," Nucl. Instr. and meth. in Phys. Res. B, **127/128** 796 (1997)

[36] X. W. Zhou, H. N. G. Wadley, "The low energy ion assisted control of interfacial structure: ion incident angle effects," Surf. Sci. Reports., **487** 159 (2001)

[37] H. Kiessig, "Interferenz von röntgenstrahlen an dünnen schichten," Ann. Phys.,**10**, 769 (1931)

[38] M. Birkholz, Thin film analysis by X-ray diffraction, Wiley-VCH, ISBN 3-527-31025-5, (2006)

[39] J. Als-Nilsson, D. McMorrow, Elements of Modern X-ray Physics, Wiley, Chichester (2000)

[40] L. A. Bendersky, F. W. Gayle, "Electrom diffraction using electron microscope", J. Res. Natl. Inst. Stand. Technol. **106**, 997 (2001)

[41] J. R. Tesmer and M. Nastasi, Handbook of modern ion beam analysis Material Reseach Society, Pittsburgh, PA (1995)

[42] U. Kreissig, S. Grigull, K. Lange, P. Nitzsche, B. SchmidtIn, "*In situ* ERDA studies of ion drift processes during anodic bonding of alkali-borosilicate glass to metal," Nucl. Inst. Meth., B **136-138,** 689 (1998)

[43] Y. Zhang, H. J. Whitlow, T. Winzell, I. F. Bubb, T. Sajavaara, J. Jokinen, K. Arstila, J. Keinonen, "Detection efficiency of time-of-flight energy elastic recoil detection analysis systems," Nucl. Instr. Meth. B **149**, 477 (1999)

[44] M. Mayer, AIP Conf. Proc. **475**, 541 (1999)

[45] T. Kingetsu, M. Yamamoto, "Growth of short-period epitaxial superlattices for X-ray multilayer mirrors," Sur. Sci. Reports., **45,** 79 (2002)

[46] K. A. Bratland, Y. L. Foo, T. Spila, H.-S. Seo, R. T. Haasch, P. Desjardins, J. E. Greene, "Sn-mediated Ge/Ge (001) growth by low-temperature molecular-beamepitaxy: Surface smoothening and enhanced epitaxial thickness," J. Appl.Phys., **97**, 044904 (2005)

[47] L. E. Murr, Interfacial Phenomnon in Metals ans Alloys, Addison-Wesley, Reading MA, (1978)

[48] H. L. Skriver, N. M. Rosengaard, "Surface energy and work function of elemental metals", Phy. Rev. B, **46**, 7157 (1992)

[49] C. Kittel, Introduction to Solid State Physics, Seventh ed., Wiley, New York, (1996)

[50] B. M. Clemens, W. D. Nix, V. Ramaswamy, "Surface-energy-driven intermixing and its effects on the measurement of interface stress," J. Appl. Phys. **87,** 2816 (2000)

[51] F. R. de Boer, R.Boom, W. C. M. Mattens, A. R. Miedemma, A. K. Niessen, Cohesion in metals: Transition metal alloys", **1**, Nort-Holland, ISBN:0 444 87098 9, (1988)

[52] B. L. Peterson, R. L. White, B. M. Clemens, "Oxygen-assisted growth of Co/Cu multilayers investigated with X-ray scattering," Physica B **336**,145 (2003)

[53] B. Kjornrattanawanich, S. Bajt, "Structural characterization and lifetime stability of Mo/Y extreme-ultraviolet multilayer mirrors," Appl.Opt., **43**, 5955 (2004)

[54] A. L. Aquila, F. Salmassi, E.M. Gullikson, F. Eriksson, J. Birch, "Measurements of the optical constants of scandium in the 50-1300 eV Range," SPIE Proceedings 5538 (2004)

[55] R. Messier, A. P. Giri, R. A. Roy, "Revised structure zone model for thin film physical structure," J. Vac. Sci. Technol. A., **2**, 500 (1984)

[56] S. Bajt "Investigation of the amorphous-to-crystalline transition in Mo/Si multilayers," J. Appl. Phys., **90**, 1017 (2001)

[57] E. M. Gullikson, F. Salmassi, A. L. Aquila, and F. Dollar, "Progress in short period multilayer coatings for water window applications," The 8th International Conference on The Physics of X-Ray Multilayer Structures (PXRMS), Sapporo, Japan, Abstract No. **S8-O4** March (2006)

[58] D. L. Windt, "Reduction of stress and roughness by reactive sputtering in W/B4C X-ray multilayer films," Proc. SPIE, 6688 (2007)

[59] D. L. Windt, "Variation in stress with background pressure in sputtered Mo/Bi multilayer films" J. Appl. Phys., **78**, 2423(1995)

[60] S. Bajt, D. G. Stearns, "High-temperature stability multilayers for extreme-ultraviolet condenser optics," Appl. Opt., **44**, 7735 (2005)

[61] T. Böttger,D. C. Meyer, P. Paufler, S. Braun, M. Moss, H. Mai, E. Beyer, " Thermal stability of Mo/Si multilayers with boron carbide interlayers," Thin Solid Films, **444**, 165 (2003)

[62] K. Le Guen, H. Maury, J.–M. Andre, P. Jonnard, A. Hardouin, F. Delmotte, M.-F. Ravet-krill, "X-ray spectroscopic application of Cr/Sc periodic multilayers," Appl. Phys. Lett. **91**, 234104 (2007)

[63] H. Stollberg, S. Yulin, P. A. C. Takman, H. M. Hertz, "High-resolution compact X-ray microscopy," Rev. Sci. Instrum. **77**, 123101 (2006)

[64] N. Ghafoor, F. Eriksson, J. Birch, "Roughness Propagation in short-period Cr/Sc and Cr/Ti Multilayers ," The 8th International Conference on The Physics of X-ray Multilayer Structures (PXRMS), Sapprao, Japan, Abstract No.**S7-04** (2006)

[65] T. Gorelik, U. Kaiser, T. Kuhlmann, S. Yulin, W. Richter, "Structural characterization of ultrathin Cr and Sc films for soft X-ray mirrors," Appl. Surf. Sci. **230**, 1 (2004)

[66] E. Majkova, Y. Chushkin, M. Jergel, S. Luby, V. Holy, I. Matko, B. Chenevier, L. Toth, T. Hatano, M. Yamamoto, "Nanometer-scale period Sc/Cr multilayer mirrors and their thermal stability," Thin Solid Films **497,** 115 (2006)

[67] W. Knulst, J. Luiten, J. Verhoeven, "Compact high-brightness soft X-ray cherenkov sources", J. Selec.Opt. Quantum Elect., IEEE, , **10**, 1414 (2004)

[68] N. Ghafoor, Fabrication and characterisation of spherically shaped multilayer X-rays mirrors, Thin Film Physics Division, IFM, Linköping University, Sweden, LiTH-IFM, EX-1155, (2003)

[69] G. Mastrogiacomo, J. Kradolfer, J. F. Löffler, "Development of magnetic Fe-based metallic glasses without metalloids," J. Appl.Phys., **99**, 023908 (2006)

[70] N. Ghafoor, F. Eriksson, P. O. A. Persson, M. Beckers, U. Kreissig, E. M. Gullikson, L. Hultman, J. Birch, "Soft X-ray Cr/Sc multilayer mirrors: Effects of B4C, O and N impurities" The 9th International Conference on The Physics of X-ray Multilayer Structures (PXRMS), Montana USA, Abstract No. **OS-2.4** (2008)

[71] J. Romero, N. Ghafoor, F. Eriksson, J. Birch, "Effects of concurrent low-energy, high-fulx ion irradiation during magnetron sputter deposition of Mo/Si multilayers," The 8th International Conference on The Physics of X-Ray Multilayer Structures (PXRMS), Sapporo, Japan, Abstract No. **PS1-13** (2006)

[72] R. van de Kruijs, E. Zoethout, A. Yakshin, I. Nedelcu, E. Louis, F. Bijkerk, H. Enkisch, G. Sipos, S. Müllender, "Nano-size crystallites in Mo/Si multilayer optics," Abstract **O136**, ICTF13/ASCIN8, (2005)

[73] J. Birch, F. Eriksson, G. A. Johansson, H. M. Hertz, "Recent advances in ion-assisted growth of Cr/Sc multilyare X-ray mirrors for the water window," Vacuum, **68**, 65 (2003)

[74] F. Eriksson, E. M. Gullikson, G. A. Johansson, J. Birch, H. M. Hertz, " 14.5% near-normal incidence reflectance for the water window", Opt. Lett., **28** 2494 (2003)

[75] A. L. Greer, "Interdiffusion in metallic multilayers", Defect and diffusion forum, **143-147,** 557 (1997)

[76] E. Hecht, Optics, 2nd edition, Addison-Wesley (1987)

[77] D. E. Kim, D. H. Cha, "Structural analaysis of a Mo/Si multilayered X-ray mirror by X-ray diffraction," J. Korean Phys. Soc. **29**, 74 (1996)

[78] H. A. Atwater, "Low energy ion surface interactions during the epitaxial growth", Solid State Phenomenon, **27,** 67(1992)

[79] D. B. Williams and C. B. Carter, Transmission Electron Microscopy, Plenum Press, New York (1996)

[80] K. P. Wellock, B. J. Hickey, M. J. Walker, N. Wiser, "The role of interface inpurities in Co/Cu giant magnetoresistance multilayers," J. Mag. and Mag. Mat., **140-144**, 586 (1995)

[81] M. Yamamoto, M, Yanagihara, A. Arai, J. Cao, T. Mizuide, H. Kimura, T. Maehara and T. Namioka, "Reflectance degradation of soft X-ray multilayer filters upon exposure to synchrotron radiation," Physica Scripta, **41,**

[82] N. Ghfaoor, Growth and nano-structural studies of metallic multilayers for X-ray mirrors, Licentiate thesis No. 1193, ISBN: 91-85457-23-X, ISSN: 0280-7971, Sweden (2005)

[83] J. DuMond, J. P. Youtz, "An X-Ray method of determining rates of diffusion in the solid state," J. Appl. Phys. **11**, 357 (1940)